



## Crustal evolution of the Paleoproterozoic Ubendian Belt (SW Tanzania) western margin: A Central African Shield amalgamation tale



Ariuntsetseg Ganbat <sup>a</sup>, Tatsuki Tsujimori <sup>a,b,\*</sup>, Nelson Boniface <sup>d</sup>, Daniel Pastor-Galán <sup>a,b,c</sup>, Shogo Aoki <sup>e,f</sup>, Kazumasa Aoki <sup>f</sup>

<sup>a</sup> Department of Earth Science, Tohoku University, Aoba, Sendai 980-8578, Japan

<sup>b</sup> Center for Northeast Asian Studies, Tohoku University, Aoba, Sendai 980-8576, Japan

<sup>c</sup> Frontier Research Institute for Interdisciplinary Sciences, Tohoku University, Aoba, Sendai 980-0845, Japan

<sup>d</sup> University of Dar es Salaam, Geology Department, P.O. Box 35052, Dar es Salaam, Tanzania

<sup>e</sup> Graduate School of International Resource Sciences, Akita University, Akita 010-8502, Japan

<sup>f</sup> Center for Fundamental Education, Okayama University of Science, Okayama 700-0005, Japan

### ARTICLE INFO

#### Article history:

Received 11 July 2020

Received in revised form 10 December 2020

Accepted 10 December 2020

Available online 24 December 2020

### ABSTRACT

The Ubendian Belt between the Archean Tanzania Craton and the Bangweulu Block, represents a Paleoproterozoic orogeny of these two constituents of the Congo Craton assembled at ~1.8 Ga, forming the Central African Shield, during the Columbia Supercontinent cycle and consolidated during the Gondwana assembly. Metagranitoids from the Southern and Northern Ufipa Terranes (Western Ubendian Corridor) and those of the Bangweulu Block are compositionally similar and are contemporaneous. The protolith of the Ufipa Terrane is originated from the collided crustal rocks of the Bangweulu Block. New LA-ICPMS zircon U-Pb age of metagranitoids and granoporphries confirmed magmatic events from 1.89 to 1.85 Ga. The metagranitoids of the Western Ubendian Corridor and that of the Bangweulu Block cannot be distinguished by their trace element characteristics and ages. Geochemically, they belong to high-K calc-alkaline to tholeiite series. The 1.89–1.85 Ga metagranitoids and granoporphries are characterized by evolved nature, which are common for slab-failure derived magmas. Such geochemical features and the presence of ~2.0 Ga eclogites suggest an Orosirian oceanic subduction and subsequent slab break-off. Melt derived from the mafic upper portion of torn slab led to the partial melting of crust which formed high-K and calc-alkaline, I- and S-type magmatism in the Bangweulu Block and the Ufipa Terrane. Zircons from two metagranites from the Northern Ufipa Terrane show Neoproterozoic (Ediacaran) overprints at ~570 Ma, suggesting the Bangweulu Block collided with the continental margin of the Tanzania Craton. However, we found non-annealed Orosirian apatites in metagranitoids from the Southern Ufipa Terrane and the Kate-Ufipa Complex, implying that areal heterogeneity of the Pan-African tectonothermal overprint in the Ufipa Terrane. All evidences suggest that the Bangweulu Block and the Ubendian Belt participated in the amalgamation of the Central African Shield as separated continents surrounded by oceanic crusts during the Paleoproterozoic Eburnean and the Neoproterozoic Pan-African orogenies.

© 2020 The Author(s). Published by Elsevier B.V. on behalf of International Association for Gondwana Research. This is an open access article under the CC BY license (<http://creativecommons.org/licenses/by/4.0/>).

### 1. Introduction

Studies on the growth and evolution of continental crust through time are fundamental to understand Earth's history. Magmatism, accretion of magmatic provinces and record of continental growth show a widely recognized episodic nature and that is apparently tied to the supercontinent cycles (e.g. Ernst et al., 2016; Pastor-Galán et al., 2019). The supercontinent cycle explains how continents amalgamate periodically into superplates that likely influence

the evolution of the lithosphere, biosphere, atmosphere and hydrosphere (Nance et al., 2014; Condie et al., 2011; Rogers and Santosh, 2003). Due to the limitations of the geological record's oldest pieces, the study of radiogenic isotopes in rocks is crucial for determining the evolution and age of the continental crust (Armstrong, 1981; Hawkesworth and Kemp, 2006). The global record of magmatic ages is likely dominated by accretion of supercontinents (Pastor-Galán et al., 2019) and the most recent data show at least five major magmatic events connected to the assemblage of supercontinents observed at ~250 Ma (Pangea), ~560 Ma (Gondwana), ~1 Ga (Rodinia), ~1.8 Ga (Columbia/Nuna) and ~2.6 Ga (Kenorland?) (Runcorn, 1962; Hawkesworth et al., 2010; Meert, 2012; Pastor-Galán et al., 2019).

\* Corresponding author at: Tohoku University, 41 Kawauchi, Aoba-ku, Sendai, Miyagi 980-8576, Japan.

E-mail address: [tatsukix@tohoku.ac.jp](mailto:tatsukix@tohoku.ac.jp) (T. Tsujimori).

During the Paleoproterozoic–Mesoproterozoic Transamazonian–Eburnean orogenies, several nuclei conformed the Congo–Sao Francisco shield (including Sao Francisco, Congo, Gabon, Angola, Kasai and Tanzania Cratons; Meert and Santosh, 2017). This shield would remain together during the amalgamation of Rodinia, Gondwana and Pangea to partially break up with the opening of the Atlantic in the Mesozoic (e.g. Torsvik et al., 2012). The Ubendian–Usagaran Belt, in east Africa, is sandwiched between the Archean Tanzania Craton and the Bangweulu Block, highly re-worked during the Pan-African orogeny (Neoproterozoic). This belt is thought to represent the Paleoproterozoic assembly of these two constituents of the Congo shield at around 1.8 Ga, during the amalgamation of Atlantica within the frame of the Columbia supercontinent cycle (e.g. Meert and Santosh, 2017). It contains a large volume of granitoids and metagranitoids with possible ages between 1.9 and 1.8 Ga (e.g. Bahame et al., 2016). However, absolute ages for granitoids along the boundary of Bangweulu Block and Ubendian Belt are scarce (Lenoir et al., 1994). Thus, the origin of the Bangweulu Block is disputed. Some authors proposed that it was an active continental margin related to the Ubendian Belt (Andersen and Unrug, 1984), whereas others supported that it formed as the result of overthickened crustal anatexis (Hanson, 2003). Recently, inferred from the absence of crustal thickening and subsequent unroofing, some studies suggested that the Bangweulu Block and Irumide Belt were metacratonized margins resulted from an attempted subduction of a passive continental margin. This subduction triggered a loss of cratonic rigidity and increased susceptibility to magmatism during subsequent deformation (De Waele et al., 2006a; Liégeois et al., 2013).

The tectonic evolution of the metagranitoids in the western margin of the Ubendian Belt is underexplored and major unknowns are: What are the geochemical characteristics of the granitoid forming magmatism and how it can constrain to processes involved in the petrogenesis, and its geodynamic setting? When did the magmatism occur? What is the extent of late Neoproterozoic metamorphism? Geochronological and geochemical studies of metagranitoids that try to decipher intracratonic crustal evolution are critical importance in understanding stabilization of continental crust.

In this research, we present new U–Pb zircon ages and whole-rock major and trace elements geochemistry of metagranitoids along two traverses across the Ufipa Terrane of the Ubendian Belt and northeastern portion of the Bangweulu Block. Our new data aim to contribute to the understanding of crustal evolution of the western margin of the Ubendian Belt, as well as, new insights on Paleoproterozoic intense magmatic events at cratonic margin and global reworking of continental crust during late Neoproterozoic time.

## 2. Geological background

Although plate kinematic constraints are limited, most researchers agree that Columbia (a.k.a. Nuna and Paleopangea, see Meert, 2012 for the naming debate) amalgamated from late Paleoproterozoic to early Mesoproterozoic (e.g. Meert and Santosh, 2017). Its maximum packing probably occurred at ~1.5 Ga (Salminen et al., 2016) and its main constituents nuclei were: Ur, Nuna (sensu Meert and Santosh, 2017) and Atlantica (Rogers and Santosh, 2002; Zhao et al., 2004; Merdith et al., 2017). Atlantica nucleus was formed after series of collisions that joined the Archean cratons of West Africa, Congo, Kalahari, Amazon, São Francisco, Rio de la Plata and Sahara (Rogers, 1996; Neves, 2011; Grenholm, 2019). The break-up of the Columbia apparently began at 1.45 Ga and continued until at least 1.38 Ga (Zhang et al., 2012; Pisarevsky et al., 2014). This break-up marked the beginning of the next supercontinent cycle, Rodinia. Rodinia supercontinent assembled between ~1.1 Ga and ~0.9 Ga (e.g. Li et al., 2008) and broke-apart at 0.8 Ga, when the Gondwana (a.k.a. Pannotia, see Nance and Murphy, 2019) cycle started. The assembly of the Gondwana commenced at ~630 Ma with the amalgamation of eastern and western Gondwana and ended about at Late Ediacaran–Early Cambrian times. Eastern

Gondwana comprised much of the present-day continents of Australia, India and East Antarctica. Whereas, western Gondwana was composed of Congo, São Francisco, Kalahari, Rio de la Plata, West Africa cratons (Meert, 2003; Collins and Pisarevsky, 2005; Oriolo et al., 2017). At ~600 Ma, the major event marking the formation of Gondwana, the Pan-African orogeny, began. The Pan-African orogeny is one of the most extensive orogenies and continental crustal reworking events occurred in the Neoproterozoic involving a long series of tectonothermal events throughout Eastern and Western Gondwana (Kröner and Stern, 2005; Meert, 2003; Veevers, 2003).

Paleomagnetic data and coeval epi-continental sequences suggest that the Congo–São Francisco Craton had been welded since ~2.05 Ga (Pedreira and De Waele, 2008; D’Agrella-Filho and Cordani, 2017). During the Paleoproterozoic–Mesoproterozoic Transamazonian–Eburnean events, the São Francisco and Central African cratons are welded to form Congo–São Francisco Craton, that would remain together during the amalgamation of Rodinia, Gondwana and Pangea (Meert and Santosh, 2017). This craton broke up with the opening of present-day South Atlantic Ocean that started in Cretaceous times (e.g. Müller et al., 2019). The Congo–São Francisco Craton experienced three Large Igneous Province events (LIP) during the Mesoproterozoic at ~1.51, ~1.39 and ~1.11 Ga (Ernst et al., 2013). The Central African cratons (Congo, Gabon, Angola, Kasai) are truncated and flanked by various orogenic belts: mid-Paleoproterozoic Ubendian–Usagaran Belt, Mesoproterozoic Kibaran (1.4–1.2 Ga) and Irumide Belt (~1.0 Ga), and highly reworked by the Pan-African orogeny (~500 Ma). These cratons are and consolidated large Central African Shield which stabilized by ~500 Ma (Cahen et al., 1984; De Waele et al., 2008; de Wit and Linol, 2015), during the assembly of Gondwana ('craton' referred as Archean nuclei; 'shield' referred as post-Archean stabilized domain).

### 2.1. Overview of the Ubendian Belt

The Ubendian Belt occupies approximately 600 × 150 km area from eastern Congo to western Tanzania and from northern Malawi to north-east Mozambique, with NW–SE trend (Fig. 1; Daly, 1988; Lenoir et al., 1994). The belt consists mainly of NW to NNW trending Paleoproterozoic granitoids and medium to high-grade metamorphosed granitoids with migmatite, mafic granulite, pelitic-psammitic gneisses, rare eclogites and ultramafic rocks, intruded by a few carbonatites with ages ranging from Mesoproterozoic to Mesozoic. On its northern end, the belt is uncomfortably overlain by rift related metasedimentary rocks of the Mesoproterozoic Kibaran Belt and Neoproterozoic Malagarasi Platform (Deblond et al., 2001; Legler et al., 2015).

The Ubendian Belt borders with the Usagaran Belt to the south-east. Together, they surround the southern margin of the Tanzania Craton. The Usagaran Belt strikes to NE–SW to E–W and is composed of continent–continent collision related metamorphic suites (migmatitic orthogneisses, pelitic-gneisses, amphibolites, and quartzites); subduction related eclogites and back arc related pillow basalts (Fig. 1). The Usagaran subduction event dates between 2.05 and 1.99 Ga indicating that it is slightly older than the 1.9–1.86 Ga Ubendian subduction event (Mruma, 1989; Möller et al., 1995; Reddy et al., 2003; Fritz et al., 2013; Boniface et al., 2012; Boniface and Appel, 2017; Mori et al., 2018; Boniface and Tsujimori, 2019; Boniface and Tsujimori, 2021). The gneissic-amphibolitic suite in the Usagaran Belt forms a basement of arc related volcanic suites and granitoids with ages between 1.92 and 1.86 Ga (Sommer et al., 2005; Manya and Maboko, 2016). Similarly, the 1.92–1.86 Ga granitoids and associated volcanics intrude into the Ubendian Belt (Lenoir et al., 1994; Kazimoto et al., 2014a, 2014b).

Three distinct Proterozoic orogenic events were recorded in the Ubendian Belt that includes: (1) the occurrences of Paleoproterozoic high-pressure rocks in the belt (Ring et al., 1997; Boniface et al., 2012), suggest that subduction and collisional events were occurred between 2.0 and 1.86 Ga. These events are concomitant with the assembly of the Atlantica amalgamation within the Columbia supercontinent

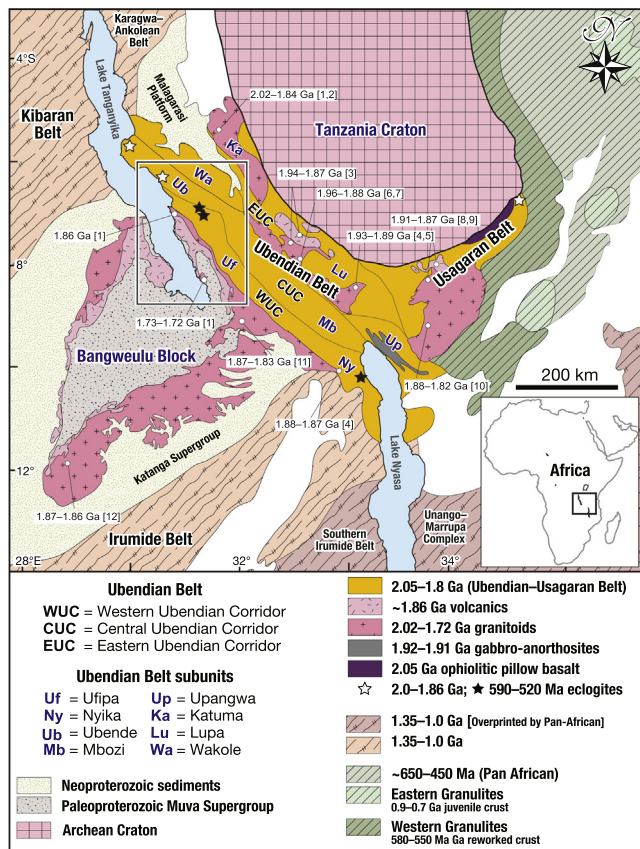


**Fig. 1.** Geological map of central-eastern Africa showing the Precambrian regional context of the Ubendian–Usagaran Belt between the Tanzania Craton and the Bangweulu Block with the magmatic ages in different terranes in the map. Corridor boundaries proposed by Boniface and Tsujimori (2021) (modified after Hanson, 2003; De Waele et al., 2006a). Paleoproterozoic magmatic ages are from: (1) Lenoir et al. (1994); (2) Kazimoto et al. (2014a, 2014b); (3) Tulibonywa et al. (2015); (4) Thomas et al. (2016); (5) Thomas et al. (2019); (6) Lawley et al. (2013a), (7) Lawley et al. (2014); (8) Sommer et al. (2005); (9) Bahame et al. (2016); (10) Manya and Maboko (2016); (11) De Waele et al. (2006b); (12) De Waele and Fitzsimons (2007). Eclogite locations and ages are adapted from Boniface et al. (2012); Boniface and Schenk (2012); Collins et al. (2004).

cycle. (2) During the Mesoproterozoic (~1.4 Ga to ~1.2 Ga), the Ubendian Belt, like the neighboring Kibaran Belt, underwent extension regime and opening of an oceanic basin (Boniface, 2019), whereas the history from ~1.2 to ~1.0 Ga, coeval with the Irumide Belt collision, probably due to far-field effect of the Rodinia assembly (Tack et al., 2010). (3) Occurrence of the Neoproterozoic eclogites (Boniface and Schenk, 2012) in the belt evinces a regional reworking during the Pan-African orogenic event and the amalgamation of Gondwana. Relicts of the abovementioned events are uniformly distributed throughout the belt.

According to Daly (1988), the Ubendian Belt consists of at least eight sub-units (terrane) characterized by unique lithological and structural features: Ubende (Ub), Wakole (Wa), Katuma (Ka), Lupa (Lu), Upangwa (Up), Mbozi (Mb), Nyika (Ny), Ufipa (Uf) (Fig. 1). Mylonitic ductile strike-slip shear zones separate one terrane from another. Theunissen et al. (1996) postulated that these terranes formed during a single dextral strike-slip movement in Paleoproterozoic time. Recent studies argued that the aforementioned terranes, formed and evolved through three discrete episodes related with oceanic subduction and collision between Tanzania, Bangweulu and Congo Cratons during the Proterozoic (Boniface et al., 2014; Boniface and Schenk, 2012; Boniface and Tsujimori, 2021). Boniface and Tsujimori (2021) clustered these terranes into three groups by similar geology and age distribution: the Western Corridor (Ufipa and Nyika), the Central Corridor (Ubende, Mbozi and Upangwa), and the Eastern Corridor (Katuma and Lupa).

The Wakole Terrane is excluded from the grouping, as it solely consists of rift-basin sediments Mesoproterozoic metasedimentary rocks without Paleoproterozoic traces (Boniface et al., 2014). The main features of internal terranes of the Ubendian Belt are briefly presented in Table 1.

## 2.2. The Bangweulu Block

The Bangweulu Block is a Paleoproterozoic cratonic region with an Archean basement component, surrounded by Proterozoic mobile orogenic belts (Fig. 1). The southern and western sides are bounded by the Mesoproterozoic Kibaran and Irumide Belts (1.35–1.0 Ga), whereas southwestern side bounded by the Neoproterozoic Lufilian Belt (880–765 Ma). The Bangweulu basement consists of three major units: (1) eastwest trending crystalline schist belt, (2) metavolcanics and granitoid batholiths, and (3) discordant intrusions. A large part of the basement is covered by the Paleoproterozoic metasedimentary sequences of the Mporokoso Group (Andersen and Unrug, 1984; De Waele et al., 2006b). The east–west trending schist belts are distributed in the northeastern and eastern part and farther west of the block and mainly consist of migmatitic biotite gneiss, biotite-epidote and muscovite gneiss, associated with mica-schist, pelitic schist, amphibolite and recrystallized quartzite.

The metavolcanics and granitoid batholiths form a corona like pattern at the margins of the Bangweulu Block intruding the schist belts (Fig. 1). Geochemically, the metavolcanics, and granitoids are characterized by high-K, calc-alkaline feature, and show negative Nb, Ta, Zr, Hf, Ti and P anomalies accompanied with positive anomalies of LILE (Large Ion Lithophile Element). Andersen and Unrug (1984) attributed the geochemical signatures of the Bangweulu metavolcanics and granitoids to their formation at the volcanic arc setting. However, De Waele et al. (2006a) suggested metacratonisation of the Bangweulu Block continental margins during the ~2.03 Ga Usagaran phase and subsequent several major reactivations in the late Usagaran phase, (~1.94 Ga), Ubendian phase (~1.87 Ga), and Lukamfwa phase (~1.6 Ga). U–Pb zircon ages for these granitoids range between 1.87 and 1.86 Ga. The  $\epsilon_{\text{Nd}}$  values are of -4.3 and -7 (volcanics) and -5.9 and -6.0 (granitoids) which gave Nd model ages, which estimate the mantle extraction age (e.g. McCulloch and Wasserburg, 1978), of 3.16–2.37 Ga (De Waele et al., 2006a; De Waele and Fitzsimons, 2007; Schandlmeier, 1983).

Whereas granites from east and south central Bangweulu Block give present-day  $\epsilon_{\text{Nd}}$  compositions of -23, -16 and model age of 3.62–2.88 Ga (Debruyne et al., 2014). These granitoids, associated with volcanic units, and mainly consist of pyroclastic rocks, minor hypabyssal intrusions and andesitic-rhyolitic flows. Volcanic rocks exhibit similar geochemical feature and rhyolites have crystallization U–Pb zircon age of 1.88–1.86 Ga (De Waele and Fitzsimons, 2007).

The Mporokoso Group of Muva Supergroup consists of weakly deformed and low-grade 5000 m thick sedimentary sequences subdivided into four formations: (1) conglomerate/diamictite, feldspathic sandstone, orthoquartzite, pelite and silicified tuffs; (2) shales and tuffs; (3) fluvialite quartizes, and mudstones, and (4) mudstones. Detrital zircon age data for the sedimentary sequence of the Mporokoso Group suggest that they deposited between 2.0 and 1.85 Ga, with a high accent on 1.87 Ga, from volcanic and plutonic source (De Waele et al., 2006b; De Waele and Fitzsimons, 2007). Maximum age constrained by granites which underlain by the Mporokoso Group and yield Rb–Sr age 1.83–1.82 Ga, whereas minimum age recorded from 1.15 Ga syenite intruding the sedimentary sequence. Archean occurrences represented by zircons with ages of 3.2, 3.0, 2.7 and 2.5 Ga (Andersen and Unrug, 1984; De Waele et al., 2006a; De Waele and Fitzsimons, 2007).

To the west from the Bangweulu Block, the Copperbelt Domes include metagranitoids and metavolcanic units similarly emplaced between 2.06 and 1.87 Ga (De Waele et al., 2006b), that were suggested westward continuation of the block within the Neoproterozoic Lufilian Belt (Rainaud et al., 2005). To the south and southeast, basement of the Mesoproterozoic Irumide Belt comprises a Neoarchean unit with

**Table 1**

Summary of geological characteristics of different terranes of the Ubendian Belt.

Corridor	Terrane	Archean-Paleoproterozoic rocks	Mesoproterozoic rocks	Neoproterozoic rocks	References
Eastern	Katuma	2.71–2.64 Ga and 2.02–1.94 Ga granitoids, metabasites, gabbro-norites; 1.94–1.8 Ga amphibolites, mafic granulites, metapelite	Syenite and quartzite, sandstone; Cu–Au–Pb ore deposits carbonate–sulphide–quartz hydrothermal veins	Sandstone, siltstone, mudstone, conglomerates of Neoproterozoic Malagarasi platform	Kazimoto et al. (2014a) Kazimoto et al. (2014b) Kazimoto et al. (2015)
	Lupa	2.7 Ga orthogneisses and granites, 1.82–1.96 Ga granitoids, gabbros, meta-andesite, –dacite, –rhyolite, 2.72 Ga, 1.96 Ga and 1.8 Ga high-grade gneiss, schistose, granite-gneiss; 1.95–1.88 Ga and gold-bearing quartz-sulfide and pyrite-gold-quartz veins	Non-foliated granite and Ngwalla carbonatite; Sediments of Mbala formation; 1.06–0.98 Ga Gold- bearing quartz-sulfide and pyrite- gold-quartz veins	Limestone, sandstone, conglomerates of Neoproterozoic Malagarasi platform	Lawley et al. (2013a) Lawley et al. (2013b) Lawley et al. (2014) Lenoir et al. (1994) Manya (2012) Thomas et al. (2019) Tulibonywa et al. (2015) Tulibonywa et al. (2017)
Central	Upangwa	1.92 and 1.91 Ga meta-anorthosite, gabbro, and pyroxenite, associated with ultramafic rocks, 2.08–1.86 Ga granitoids; metapelites	Andesitic lava (1.67 Ga), syenites; orthogneiss, metapelite migmatites, amphibolites	Potassic granite (724 Ma)	Boniface and Appel (2018) Boniface (2020) Manya and Maboko (2016) Thomas et al. (2016)
	Mbozi	1.88–1.87 Ga granitoids; 1.81 Ga granulite-amphibolite suite, associated with amphibolite to granulite facies metasedimentary rocks, quartzo-feldspathic gneisses		Mbozi gabbro (743 Ma)	Brock (1968) Bingen et al. (2009) Lenoir et al. (1994) Ray (1974)
Ubende		Bt granite, gabbro-norite, ultrabasites (pyroxenites), serpentinized peridotite; 1.89–1.87 Ga MORB-type eclogite, 1.83–1.81 Ga metapelite; Metasediments interlayered with quartzite, Grt-Bt-Ms gneiss/schist, quartzite	Carbonatites and syenite-porphry	Mylonitization of eclogite in 600–570 Ma	Boniface et al. (2012) Boniface and Tsujimori (2021) Wilhelmiij and Cabri (2016)
	Ufipa	Metagranitoids, Kate–Ufipa non foliated granitoids and Kipili volcanics; 1.9 Ga Bt–Grt–Ky/Sil gneiss/schist, migmatites, quartzite, amphibolite layers, metabasite layers, kyanite eclogite, charnockites	Conglomerate, sandstone and siltsone of Mbala formation	593–524 Ma kyanite-free eclogite lenses in gneisses; 566–556 Ma metapelite gneisses	Boniface et al. (2012) Boniface and Appel (2018) Boniface and Schenk (2012) Boniface and Tsujimori (2021)
Western	Nyika	2.00–1.93 Ga meta-granitoids and enderbites associated with Crd-Sil gneisses; Crd-Sil granulites, Grt-Sil-Bt gneiss/schist, migmatites, quartzite, Hbl-gneisses/schists	1.1–1.0 Ga A-type granites and plume basalt; 944 Ma metapelite	530–500 Ma eclogite; 559–554 Ma metapelite	Ring et al. (1997) Ring et al. (2002) Boniface and Appel (2017)
	Wakole		Pt bearing mafic-ultramafic igneous complex; 1.16–1.06 Ga metasediments		Boniface et al. (2014)

igneous crystallization age of ~2.61 Ga, and various ~2.03 and ~1.97 Ga gneisses (De Waele et al., 2006a; Debruyne et al., 2014). The evidence of the Archean basement in the Bangweulu Block is recorded by the Mesoarchean (~3.2 Ga) xenocrystic and detrital zircon within a ~1.8 Ga lapilli tuff (Rainaud et al., 2003) and 2.76 Ga tonalite-trondjhemite–granodiorite suite (De Waele et al., 2006a, 2006b).

### 2.3. Study area

The study area straddles the boundary of the Ufipa Terrane and the northeastern margin of the Bangweulu Block along the eastern shore of Tanganyika Lake (Fig. 2). The boundary is delineated by a shear zone and metamorphic grade transition from chlorite-muscovite-biotite schist from the central part of the Bangweulu Block to sillimanite-cordierite gneisses and amphibolite towards the Ubendian Belt (Andersen and Unrug, 1984; De Waele et al., 2006b). Recognizing this contact is not easy, as the contact zone is intruded by numerous granitic intrusions of the Paleoproterozoic Kate–Ufipa Complex. The Kate–Ufipa Complex consists mainly of deformed plutonic rocks, including coarse-grained porphyritic granite, biotite-granite, granodiorite, plagiogranite, tonalite and syenogranite. Volcanic equivalents of the Kate–Ufipa Complex is represented by the Kipili volcanics. Lithologies show spatial variation, with dacitic and rhyodacitic tuffs and the few andesites dominating to the south, whereas rhyolitic tuffs, flows, and ignimbrites become more frequent to the north and east (Lenoir et al., 1994; Nanyaro et al., 1983). Based on metamorphic mineral assemblages in gneisses, Boniface and Appel (2018) subdivided the Ufipa Terrane into

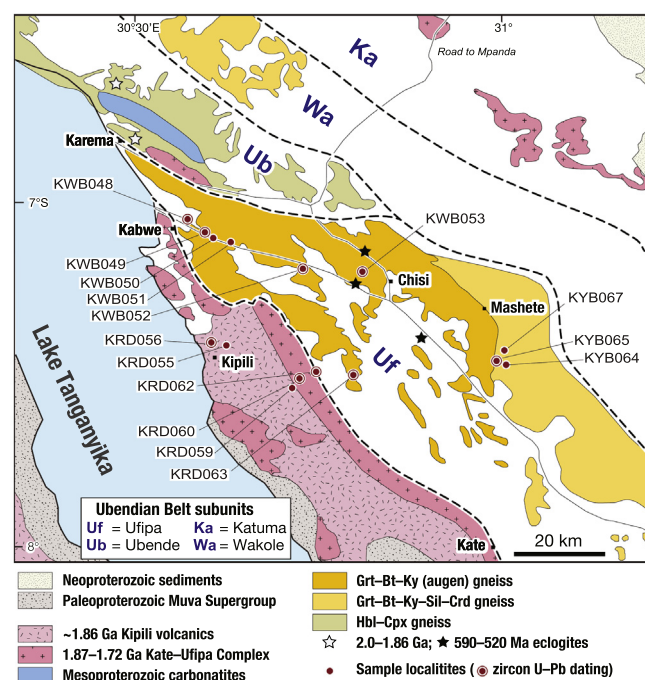


Fig. 2. Local geological map of the northern part of the Ufipa Terrane and northeastern portion of the Bangweulu Block and location of samples used in this study.

**Table 2**

Location and mineral assemblage of the metagranitoids and granoporphries from the Ubendian Belt and northeastern portion of the Bangweulu Block.

Samples	KRD063	KWB052	KRD056	KBW048	KWB053	KYB065	KWB049	KRD060	KRD062	KRD059	KRD061	KRD064	KWB050	KRD055	KWB052b	KYB067
Rock name	Metagranite	Metagranite	Grano- porhyry	Metagranite	Metagranito- diorite	Metamono- granite	Metagranodiorite	Metamono- granite	Metagrano- diorite	Grano- porhyry	Metagrano- diorite	Metagranite	Metamono- granite	Grano- porhyry	Metamono- granite	Metagrano- diorite
Location	Latitude	7.46510S	7.16850S	7.43170S	7.04945S	7.17345S	7.44257S	7.06965S	7.46687S	7.44685S	7.47892S	7.46042S	7.44335S	7.08233S	7.16850S	7.43917S
	Longitude	30.924E	30.80930E	30.63188E	30.55488E	30.90333E	31.16765E	30.60182E	30.81453E	30.83963E	30.80085E	30.82097E	31.16747E	30.63472E	30.80930E	31.16690E
Major minerals	Quartz	xx	xxx	xx	xxx	x	xxx	xx	xxx	xx	xxx	xx	xxx	xx	xx	xxx
	K-feldspar	xx	xxx	xx	xxx	x	xxx	xx	xxx	xx	xx	xx	xx	xx	xx	x
	Plagioclase	xx	xx	x	xx	xxx	x	xxx	xxx	xxx	xxx	xxx	xx	xxx	xx	xxx
	Hornblende	x	x	x	xx	x	xx	xx	x				x		x	x
	Biotite	x	x	x	xx	x	xx	x	x	xx	x	xx	xx	x	xx	x
	Muscovite	x	x	x	x	x	x	x					xx		x	
Accessory and metamorphic minerals	Chlorite	+														
	Epidote	++														++
	Garnet	++	++													++
	Kyanite															
	Ilmenite		+													+
	Rutile															
	Titanite	++	+	+				++		+	+				+	+
	Apatite	+	+	+	+	+	+	+	+	+	+	+	+	+	+	+
	Magnetite															
	Zircon	++	++	++	++	++	++	++	++	++	+	+	+	+	+	+
	Allanite															+

xxx Mineral content &gt; 30%; xx Mineral content &gt; 10–30%; x Mineral content &lt; 10%.

++ Abundant accessory/secondary mineral; + Rare accessory/secondary mineral.

the northern and southern parts. The Northern Ufipa Terrane consists mainly of kyanite-bearing biotite-granitic gneisses, semi-metapelitic to metapelitic gneisses, and metagranites, with minor eclogites and high-pressure granulites; the occurrence of kyanite-bearing gneiss and eclogites suggest relatively high-pressure metamorphic regimes. In contrast, the Southern Ufipa Terrane is characterized by low pressure

metamorphic regimes, composed of sillimanite-bearing biotite-rich granitic gneisses, semi-pelitic to metapelitic migmatites. Metapelites and gneisses of the both Northern and Southern Ufipa Terranes yielded zircon and monazite metamorphic ages of 1.96–1.90 Ga and of 599–537 Ma. We collected deformed granitoid samples from both the Northern and Southern Ufipa Terrane and weakly deformed granitoids from the

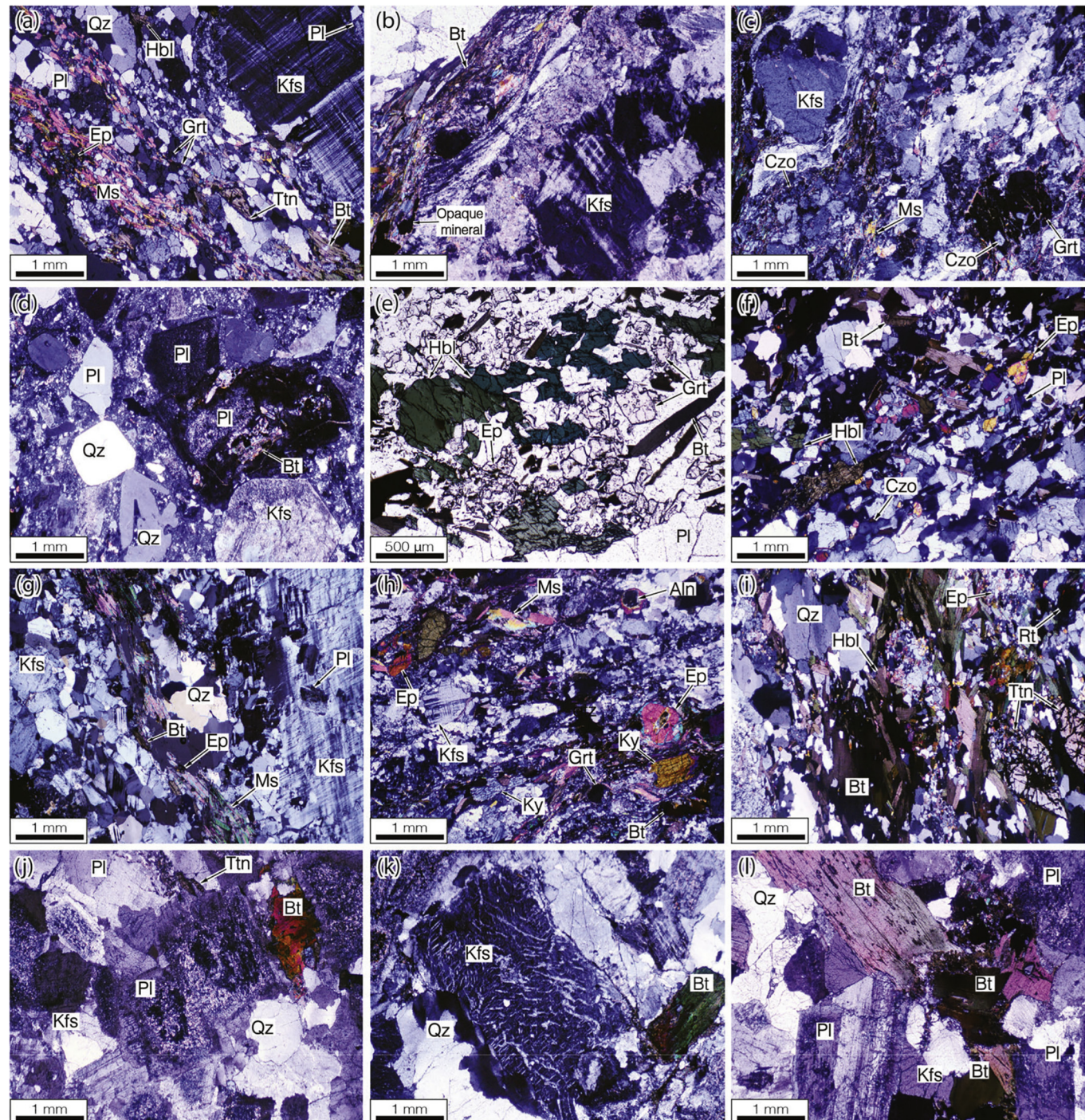


**Fig. 3.** Photomicrographs of the age-dated samples. (a) Sample KRD063 showing a deformed feature; the sample contains garnet and epidote [XPL (cross-polarized light view)]. (b) Sample KWB052 showing a deformed feature; K-feldspar exhibits pericline [XPL]. (c) The occurrence of garnet in the sample KWB052 [XPL]. (d) Sample KRD056 showing phenocrysts of quartz and plagioclase in fine-grained matrix [XPL]. (e) Sample KWB053 showing the occurrence of hornblende, epidote and garnet [PPL (plane polarized light view)]. (f) Sample KWB053 showing a foliation defined by a preferred-orientation of hornblende [XPL]. (g) Sample KWB048 showing a large K-feldspar with cross-hatched twinning [XPL]. (h) Sample KYB065 showing the occurrence of kyanite [XPL]. (i) Sample KWB049 showing the occurrence of biotite and hornblende. (j) Sample KRD060 showing the occurrence of partially-altered plagioclase. (k) K-feldspar with perthite texture in KRD062 [XPL]. (l) The occurrence of undeformed biotite in KRD062 [XPL]. (For interpretation of the references to color in this figure legend, the reader is referred to the web version of this article.)

Kate-Ufipa Complex (KRD060–062) as well as granoporphries from the Kipili metagranitoids (KRD055–056, 059). Locations and lithologies of the studied samples are shown in Table 2 and Fig. 2.

### 3. Methods

#### 3.1. Whole-rock geochemistry

A total of sixteen metagranitoid samples was selected for whole-rock major and trace element chemistry. The analyses were carried out at Activation Laboratories Ltd., Canada, using Code 4Lithoresearch Lithogeochemistry Package; the package uses lithium metaborate/tetraborate fusion with inductively coupled plasma optical emission spectrometry (FUS-ICPOES) and inductively coupled plasma mass spectroscopy (FUS-ICPMS) for the major and trace element analyses, respectively.

#### 3.2. U-Pb geochronology

Zircons were separated from the nine whole-rock samples using conventional rock-crushing, heavy liquid and magnetic techniques, and by handpicking under a binocular microscope. The handpicked zircons are mounted in epoxy resin (Struers Specifix-40) discs and polished until the zircon interiors were exposed and examined by transmitted and reflected light with an optical microscope. A Metkon Forcipol 1 V and a 3 M aluminum oxide lapping film was used for the polishing. To reveal their internal structures, cathodoluminescence (CL) images were obtained using a Hitachi S-3400 N SEM, equipped with a Gatan model MiniCL system housed at the Graduate School of Science, Tohoku University, Japan (Fig. 10). The CL observation was conducted using 25 kV accelerating voltage and a 90 nA probe current. Distinct domains within the zircons were selected for analysis, based on the CL images. In situ zircon U–Pb dating was carried out in the Okayama University of Science by using a Thermo Fisher Scientific iCAP-RQ single-collector quadrupole coupled to a Teledyne Cetac Technologies Analyte G2 ArF excimer laser ablation (LA) system equipped with a HelEx 2 volume sample chamber. The laser ablation of zircons was conducted at the condition of laser spot size of 25 μm, fluence of 1.8 J/cm<sup>2</sup> and repetition rate of 5 Hz. Other conditions of LA-ICPMS method are referred to Aoki et al. (2019) and Aoki et al. (2020). The zircon 91,500 (1065 Ma; Wiedenbeck et al., 2004) was used as an external standard for age calibration, and the NIST SRM 612 (Jochum et al., 2011) silicate glass was applied for instrument optimization, and the Plešovice zircons (337 Ma; Sláma et al., 2008) were measured as secondary standards for quality control. U–Pb ages and concordia diagrams were calculated and drawn using the programs IsoplotR (ver. 3.75; Vermeesch, 2018), concordia age of each sample incorporates errors on the decay constants and includes evaluation of concordance of apparent ages. The concordia ages and errors are at the two-sigma level.

### 4. Results

#### 4.1. Petrography

**Sample KRD063:** Metagranite, porphyroblastic, lepidoblastic, granoblastic in texture (Fig. 3a), contains K-feldspar-microcline (~20%), plagioclase (~20%), quartz (~25%), biotite + muscovite (~20%), and hornblende (~5%). Metamorphic minerals are epidote (clinzoisite and others) and garnet (5%). Accessory and secondary minerals (~5%) are characterized by titanite, zircon, apatite and opaque minerals probably altered from mafic minerals. Poikiloblastic texture is presented by idioblastic microcline megacrysts with cross-hatched twinning containing relicts of quartz, and plagioclase.

**Sample KWB052:** Metagranite, porphyroblast, lepidoblast in texture, composed of K-feldspar (~30%), quartz (~30%), plagioclase (~10%), biotite (~10%), hornblende (~10%) and subordinate (~5%) garnet, epidote,

and chlorite. Accessory minerals (~5%) are zircon, apatite, titanite, and muscovites (Fig. 3b). Subidioblastic K-feldspars exhibit cross-hatched and pericline twinning. Pericline twinning occurs as the result of monoclinic orthoclase or sanidine transforming to microcline. Plagioclase markedly altered to clay minerals and biotite to epidote. Porphyroblastic garnet with skeletal texture containing ilmenite, clinzoisite as an inclusion (Fig. 3c). Quartz, biotite, and muscovites are form shape preferred orientations.

**Sample KRD056:** Granoporphry, porphyritic, hypocrystalline in texture, composed of phenocrysts K-feldspar (~20%), quartz (~20%), plagioclase (~10%) and cryptocrystalline groundmass minerals (~50%), which consist of felsic minerals, devitrified volcanic glass, biotite and accessory and secondary minerals such as epidote, zircon and apatite (Fig. 3d). The phenocrysts, mainly idiomorphic, variably exhibit corroded embayment of rhyolitic quartz. Feldspars are altered to clay minerals, display faint carlsbad and cross-hatched twinning. Some megacrystals contained plagioclase, zircon, epidote, and altered biotite. Plagioclase crystals are sericitized. Biotites often lobed in the periphery of phenocrysts and altered to sericite and epidote.

**Sample KWB053:** Metagranodiorite, lepidoblastic, granoblastic in texture comprised plagioclase (~30%), hornblende (~20%), biotite (~20%), K-feldspar (~10%), quartz (~10%), zircon and apatite. Epidote, garnet, and clinzoisite occur as metamorphic minerals (~10%). Idioblastic to subidioblastic hornblende crystals demonstrate clear diamond-shape cleavage (Fig. 3e), often clustered with biotite laths. Unlike other samples, in subidioblastic plagioclase crystals of this sample are able to determine composition which is identified as an anorthite (An45[average]). This association is largely replaced by felty masses of epidotes (Fig. 3f; clinzoisite and others). Possibly, by breakdown of anorthite component in plagioclase formed albite and clinzoisite, magmatic hornblende breakdown formed epidotes.

**Sample KWB048:** Metagranite, porphyroblastic, lepidoblastic, granoblastic in texture (Fig. 3g), contains K-feldspar (~30%), quartz (~30%), biotite + muscovite (~20%), plagioclase (~15%), and hornblende (~5%). Zircon and apatites make up to ~1% as accessory minerals. Subidioblastic to xenoblastic potassic feldspar-microcline with cross-hatched and simple twinning occurs as porphyroblastic minerals. Poikilitic texture is presented by microcline containing quartz, and plagioclase, indicating that microcline formed after plagioclase crystals. Cluster of muscovite and brownish biotite laths contain subhedral epidote prisms. Hornblendes are rarely present. The rock contains a penetrative schistosity defined by micas.

**Sample KYB065:** Metamonzogranite, heteroblastic in texture (Fig. 3h), which constituents represented by K-feldspar (~30%), plagioclase (~10%), quartz (~40%), muscovite (~10%), biotite (~10%) and minor zircon, apatite and ilmenite. Garnet, clinzoisite, and kyanite occur as metamorphic minerals. Epidotes form large rounded crystals with cores of allanite, which served as crystallization seeds, it is often surrounded by oriented biotite, and muscovite. Sub- to xenomorphic potassic feldspars sandwiched by recrystallized quartz.

**Sample KWB049:** Metagranodiorite, porphyroblastic and lepidoblastic in texture (Fig. 3i), consisting of K-feldspar (~20%), plagioclase (~30%), quartz (~20%), hornblende (~20%), biotite (~5%), muscovite (~5%). Accessory minerals are titanite, apatite, zircon and rutile. Metamorphic minerals are epidote (and clinzoisite) and kyanite. Microclines and plagioclases occur as porphyroblastic minerals and often corroded by quartz. Two types of quartz are presented: porphyritic and interstitial. Porphyroblastic grains surrounded by micas and hornblende which define schistosity of sample. Plagioclase is saussuritized and largely replaced by felty masses of epidote, muscovite.

**Sample KRD060:** Metamonzogranite weakly foliated, hypidiomorphic granular in texture, consists of plagioclase (~30%), K-feldspar (~30%), quartz (~30%) and biotite (~10%). Accessory minerals are represented by zircon and apatite. Euhedral plagioclase occurs as tabular crystals with zonation and slightly elongated with polysynthetic twinning and they are sericitized in the core part (Fig. 3j), which implies

**Table 3**

Major element (wt%) and trace element ( $\mu\text{g/g}$ ) compositions of the metagranitoids and granoporphyries from the Ubendian Belt and northeastern portion of the Bangweulu Block.

High-K calc-alkaline metagranitoids										Calc-alkaline metagranitoids			Granoporphyries			
Sample	KWB048	KWB049	KWB050	KWB052	KWB052b	KWB053	KRD063	KRD060	KRD061	KRD062	KYB064	KYB065	KYB067	KRD055	KRD056	KRD059
SiO <sub>2</sub>	72.77	61.55	67.09	74.39	73.17	61.43	70.20	69.35	67.97	62.33	78.19	70.83	66.90	72.46	70.33	69.75
TiO <sub>2</sub>	0.18	0.78	0.52	0.17	0.36	0.84	0.44	0.35	0.52	0.82	0.56	0.67	0.59	0.28	0.33	0.49
Al <sub>2</sub> O <sub>3</sub>	13.9	17.7	15.0	12.4	12.4	15.3	14.5	14.5	15.4	16.4	10.2	13.3	15.2	12.7	13.5	14.3
FeO	1.01	4.7	3.55	1.64	2.38	6.62	2.14	2.32	3.13	5.78	4.81	5.53	5.17	2.53	2.94	2.55
MnO	0.03	0.1	0.07	0.05	0.03	0.12	0.05	0.06	0.08	0.11	0.07	0.09	0.1	0.05	0.05	0.08
MgO	0.25	1.52	1.09	0.31	0.63	2.79	0.53	0.55	0.82	1.77	1.08	1.77	1.86	0.31	0.49	0.36
CaO	1.37	5.21	3.20	1.07	1.23	5.20	2.12	2.33	2.89	4.50	1.35	1.59	1.62	0.56	2.48	1.62
Na <sub>2</sub> O	3.06	4.31	3.26	2.83	2.80	2.97	3.15	3.45	3.57	3.41	1.97	1.65	4.13	2.21	3.18	4.00
K <sub>2</sub> O	5.26	2.35	4.43	5.26	4.88	2.52	5.08	4.34	3.79	3.54	0.88	2.67	2.29	5.37	3.80	4.17
P <sub>2</sub> O <sub>5</sub>	0.03	0.21	0.17	0.04	0.07	0.25	0.13	0.08	0.19	0.29	0.03	0.05	0.10	0.06	0.09	0.12
LOI	1.00	1.25	1.09	1.50	1.05	1.26	0.83	1.27	1.54	0.94	0.72	1.39	1.06	1.59	1.89	2.36
Total	98.81	99.63	99.42	99.62	98.99	99.34	99.21	98.55	99.87	99.87	99.81	99.52	99.05	98.15	99.12	99.84
Rb	178	69	131	121	119	105	114	144	130	117	18	79	84	167	121	119
Sr	238	701	476	457	427	456	436	341	483	570	247	320	171	195	364	265
Y	14.4	34.0	26.6	18.7	7.5	24.4	87.9	25.1	25.5	28.6	12.1	23	29.7	23.8	21.2	77.8
Cs	1.0	1.5	1.8	0.4	0.6	1.7	1.2	1.7	2.6	1.7	0.1	0.5	1	3.1	2.0	2.0
Ba	978	1183	1476	1344	1399	1288	2292	1048	1438	1290	234	1495	565	1454	1085	1658
La	33.6	54.8	54.0	29.5	49.3	88.4	47.6	47.6	28.4	51.9	42.1	88.7	62.1	71.3	43.2	154
Ce	58.4	115	115	56.7	95.2	159	107	96	80.2	109	70.9	83.3	123	111	85.7	101
Pr	6.11	13.4	12.3	6.02	10.2	17.6	16.3	10.3	6.2	12.0	7.83	16.5	13.8	15.1	9.33	23.0
Nd	18.9	49.7	41.5	20.5	34.3	59.6	64.5	34.6	22.1	45.0	26.6	54.2	48.5	50.6	31.2	79.0
Sm	3.27	9.30	7.14	3.62	5.43	9.61	14.5	5.98	4.98	8.69	4.13	8.21	8.72	8.50	5.50	12.6
Eu	0.65	2.21	1.57	0.57	1.10	1.8	2.43	1.2	1.3	1.96	1.05	2.23	1.69	1.46	1.18	2.86
Gd	2.43	7.58	5.56	2.7	3.53	7.39	12.7	4.83	4.04	6.55	2.89	5.63	7.44	5.79	4.28	12.8
Tb	0.36	1.07	0.8	0.43	0.41	1.03	2.35	0.72	0.63	0.97	0.39	0.72	1.1	0.79	0.65	1.86
Dy	2.21	6.2	4.63	2.82	1.87	5.04	14.9	4.46	3.72	5.39	2.28	4.19	6.14	4.33	3.85	11.1
Ho	0.47	1.18	0.90	0.69	0.30	0.87	3.14	0.84	0.80	1.01	0.43	0.80	1.15	0.81	0.75	2.32
Er	1.36	3.39	2.64	2.36	0.71	2.37	9.21	2.52	2.33	2.94	1.21	2.40	2.88	2.49	2.20	6.56
Tm	0.21	0.48	0.40	0.38	0.09	0.32	1.28	0.37	0.33	0.42	0.16	0.34	0.38	0.38	0.35	0.87
Yb	1.56	3.17	2.59	2.74	0.52	1.88	7.31	2.61	2.21	2.64	1.03	2.43	2.28	2.52	2.27	5.11
Lu	0.27	0.48	0.41	0.4	0.09	0.32	1.0	0.41	0.39	0.39	0.18	0.38	0.34	0.41	0.36	0.76
Pb	23	14	19	42	32	21	18	21	20	15	21	10	25	26	20	20
Th	15.7	7.32	11.1	12.4	13.6	16.2	6.45	13.3	14	20	4.86	9.27	26.4	16.7	12.8	13.7
U	2.18	1.63	1.62	0.67	1.24	0.79	1.16	3.1	2.49	2.15	0.62	0.53	0.95	2.74	2.57	2.71
Zr	98	291	215	123	129	153	222	155	267	263	217	264	157	138	151	271
Nb	6.0	10.2	8.2	2.2	4.1	8.6	10.3	9.0	10.1	12.0	6.3	5.7	7.7	7.5	8.2	11.2
Hf	3.0	6.7	5.3	3.7	3.3	4.1	5.8	4.3	7.2	7.3	6.0	6.8	4.2	4.6	4.4	6.7
Ta	0.65	0.76	0.94	0.13	0.27	0.32	1.39	0.96	0.77	0.78	0.22	0.44	0.40	0.89	0.80	0.88
Sc	3	14	12	4	5	22	4	6	8	13	9	14	13	4	5	7
Cr	20	20	20	20	20	70	20	20	20	30	100	110	60	20	20	20
Co	1	10	8	2	4	18	3	4	2	12	10	16	13	2	4	3
Ni	20	20	20	20	20	40	20	20	20	20	20	30	30	20	20	20
Zn	30	60	40	30	30	80	30	30	40	60	50	70	80	40	40	40
Ga	13	19	16	10	13	21	15	16	18	19	14	18	18	15	16	15
Tl	0.7	0.26	0.43	0.45	0.49	0.39	0.43	0.44	0.51	0.43	0.16	0.29	0.28	0.71	0.39	0.41
K <sub>2</sub> O/Na <sub>2</sub> O	1.72	0.55	1.36	1.86	1.74	0.85	1.61	1.26	1.06	1.04	0.45	1.62	0.55	2.43	1.19	1.04
A/CNK	0.85	0.92	0.94	1.01	1.02	0.90	1.00	0.99	1.01	0.93	1.53	1.56	1.25	1.22	0.98	1.02
Mg#	30.66	36.58	35.34	25.23	32.10	42.89	30.61	29.69	31.82	35.32	28.6	36.35	39.05	17.94	22.89	20.13
Zr/Nb	16.33	28.53	26.22	55.91	31.46	17.79	21.55	17.22	26.44	21.92	34.44	46.32	20.39	18.4	18.41	24.2

(continued on next page)

**Table 3** (continued)

High-K calc-alkaline metagranitoids										Calc-alkaline metagranitoids				Granoporphries		
Sample	KWB048	KWB049	KWB050	KWB052	KWB053	KRD060	KRD061	KRD062	KYB064	KYB065	KYB067	KRD055	KRD056	KRD059		
[La/Yb] <sub>CN</sub>	15.45	12.4	14.96	7.72	68.01	33.73	4.67	13.08	9.22	14.1	29.32	26.18	19.54	20.3	13.65	21.62
[La/Sm] <sub>CN</sub>	6.42	3.68	4.72	5.09	5.67	5.74	2.05	4.97	3.56	3.73	6.37	6.75	4.45	5.24	4.90	7.63
[Nb/La] <sub>PW</sub>	0.18	0.19	0.15	0.07	0.08	0.10	0.22	0.19	0.36	0.23	0.15	0.06	0.12	0.11	0.19	0.07
Eu/Eu*	0.08	0.03	0.04	0.06	0.06	0.03	0.01	0.04	0.07	0.03	0.09	0.05	0.05	0.03	0.05	0.02
[Th/Ta] <sub>PW</sub>	24.2	9.6	11.8	95.4	50.4	50.6	4.6	13.9	18.2	25.6	22.1	21.1	66.0	18.8	16	15.6
[Th/La] <sub>PW</sub>	4.04	1.15	3.63	2.38	1.58	1.17	2.41	4.26	3.3	0.99	0.93	3.67	2.02	2.56	0.76	
Th/Nb	2.62	0.72	1.35	5.64	3.32	1.88	0.63	1.48	1.39	1.67	0.77	1.63	3.43	2.23	1.56	1.22
[Hf/Ta] <sub>PW</sub>	4.62	8.82	5.64	28.46	12.22	12.81	4.17	4.48	9.35	9.36	27.27	15.45	10.5	5.17	5.5	7.61

Total Fe as FeO.  
 $Mg\# = 100 \times Mg/(Mg + Fe)$  atomic.  
 $Eu^* = Eu_{CN}/(Sm_{CN} \times Gd_{CN})^{1/2}$ .

plagioclase zonation is varying from albite core to more calcic to rim. Euhedral to subhedral microcline displays cross-hatched twinning, perthite intergrowth (Fig. 3k), where albite replaces microcline or orthoclase, rarely poikilitic texture presented containing quartz crystals. Anhedral, interstitial quartz filled gaps between feldspars. Biotite laths partially altered to muscovite and clinozoisite.

*Sample KRD062:* Metagranodiorite, weakly foliated, hypidiomorphic granular in texture (Fig. 3l), consists of plagioclase (~30%), K-feldspar (~15%), quartz (~20%), biotite (~20%) and hornblende (~10%). Accessory and secondary minerals (~5%) include titanite, zircon and apatite. Euhedral to subhedral plagioclase crystals are show simple and polysynthetic twinning. Brownish biotite laths are pervasively corroded by feldspar along its periphery and replaced by opaque minerals and chlorite.

#### 4.2. Whole-rock geochemistry

The major and trace element geochemical data of the studied metagranitoids including granoporphries are given in Table 3. On the basis of major element characteristics, the samples can be divided into high-K calc-alkaline and calc-alkaline granitoids regardless of deformation. Hence, hereafter weakly foliated granitoids, Grt–Bt–Ky augen gneisses and weakly foliated granoporphries are referred to high-K metagranitoids, and Grt–Bt–Ky–Sil–Crd gneisses are referred to calc-alkaline metagranitoids.

##### 4.2.1. Alteration and element mobility

Since studied rocks have been affected by metamorphism and sericite alteration, prior to petrogenetic interpretation of major and trace element content, it is essential to ensure whether they have triggered significant post-magmatism element mobility. All of the metagranitoids and volcanic rock samples have low Loss of Ignition (LOI) values (all < 2.36%), and show their relatively low contents of weathering or alteration minerals (e.g. carbonate, hydrous minerals). Moreover, poor correlation has been shown between LOI and Eu anomaly ( $= 0.2$ ; Eu/Eu\*) and Sr ( $= 0.1$ ), indicating Sr or Eu anomaly is not significantly affected by post-emplacement processes. To assess the element mobility, we compare high field strength elements (HFSE) and rare earth element (REE), considered as immobile during metamorphic processes, against the large ion lithophile elements (LILE), which are mobile during secondary processes (Polat and Hofmann, 2003).

The bivariate plots for the Zr (sensitive indicator of immobility) versus Na<sub>2</sub>O and Ce show scattered points and poor correlation ( $R^2 < 0.3$ ), which suggests it was likely affected by secondary processes (not shown), whereas Zr versus REE (represented by Sm) (Fig. 4a), HFSE (represented by Hf) (Fig. 4b), LILE (represented by Rb) (Fig. 4c) demonstrated a relatively linear trend with moderate to good correlations ( $R^2 = 0.46$ –0.96), suggesting that they are not much affected by secondary processes. We interpreted our geochemical analyses avoiding those elements that show mobility during secondary processes. When plotting samples on major element discrimination diagrams and on bivariate diagrams, samples exhibit two different trends (Figs. 5 and 6), especially regarding K<sub>2</sub>O.

##### 4.2.2. Calc-alkaline metagranitoids

Calc-alkaline metagranitoids fall in the granodiorite and granite fields in the total alkali-silica (TAS) diagram (Fig. 5a; Irvine and Baragar, 1971). They have high SiO<sub>2</sub> contents, between 66.9 and 78.2 wt% (average = 70.9 wt%), and moderate to high Al<sub>2</sub>O<sub>3</sub> contents, between 10.2 and 15.2 wt% (average = 13.5 wt%). Their molar Al<sub>2</sub>O<sub>3</sub>/[CaO + K<sub>2</sub>O + Na<sub>2</sub>O] (A/CNK) values range from 1.25 to 1.56, indicative of peraluminous metagranitoids (Fig. 5b). They have narrow range of Fe-numbers between 0.82 and 0.91 (Fe#, calculated as FeO<sup>T</sup>/(FeO<sup>T</sup> + MgO) [FeO<sup>T</sup>: total Fe as FeO]) and Mg-number [Mg#, calculated as 100 × Mg/(Mg + Fe)] vary from 28 to 39 and plot on magnesian field on Fe# versus SiO<sub>2</sub> diagram (Fig. 5c; Frost et al., 2001). They have moderate

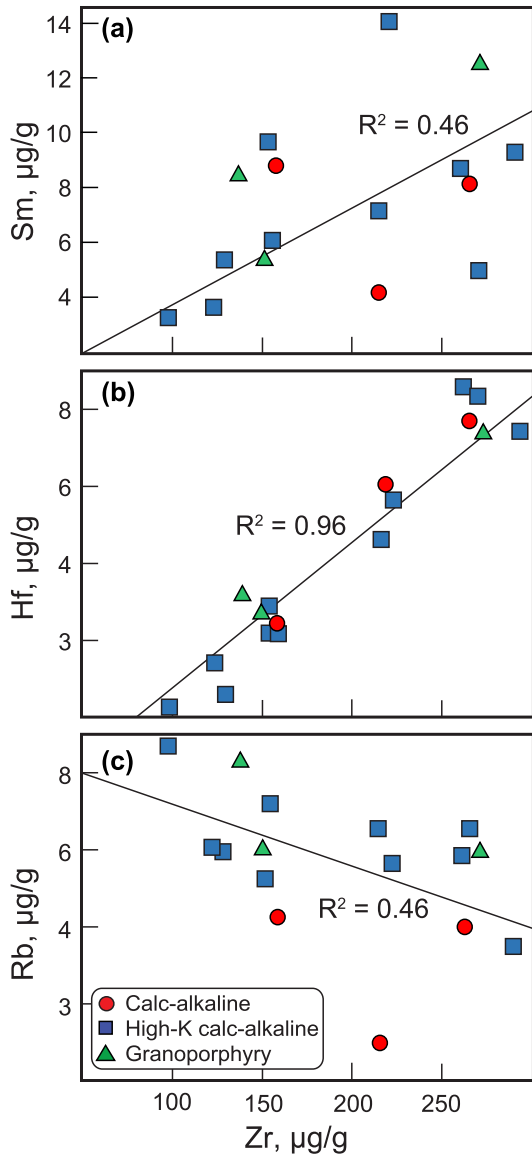


**Fig. 4.** Plot of Zr versus (a) Sm, (b) Hf and (c) Rb for the metagranitoids including granoporphyries and corresponding correlation coefficient.

content of  $K_2O$  (0.88–2.67), thus they are classified as calc-alkaline to tholeiitic rock (Fig. 5d; Peccerillo and Taylor, 1976). They contain high  $TiO_2$  (0.56–0.67 wt%),  $MgO$  (1.08–1.86 wt%),  $FeO^T$  (4.81–5.17 wt%),  $MnO$  (0.07–0.10 wt%), Cr (60–110 µg/g) and low Sr (171–320 µg/g), and show irregular variation on Harker binary diagrams (Fig. 6).

On CI-chondrite normalized REE diagrams (Fig. 7a), metagranitoids share many geochemical features with the upper crust, and show enrichment of the LREE relative to HREE ( $[La/Yb]_{CN} = 19.5\text{--}29.3$ ; CN represents chondrite normalized values). They exhibit weak Eu anomalies ( $Eu/Eu^* = 0.03\text{--}0.09$ ). On primitive mantle normalized multi-element diagrams (Fig. 7b), metagranitoids are characterized by elevated concentrations of Rb, Ba, Th and Pb and depletion in Nb, Ta and Ti ( $[Nb/La]_{PM} = 0.06\text{--}0.15$ , where PM represents primitive mantle normalized values), and enrichment of the LREE ( $[Th/La]_{PM} = 0.9\text{--}3.6$ ) comparing to the adjacent elements. They are plotted on volcanic arc granite field on Rb versus Ta + Yb (Fig. 8a) and Nb versus Y diagrams (Fig. 8b).

#### 4.2.3. High-K calc-alkaline metagranitoids and granoporphyries

According to the TAS diagram (Irvine and Baragar, 1971), high-K calc-alkaline metagranitoids including granoporphyries are mostly

granitic in composition, with minor granodiorite and diorite (Fig. 5a). Their  $SiO_2$  contents range between 61.4 and 74.3 wt% (average = 67.7 wt%), and they have moderate to high  $Al_2O_3$  contents range between 12.4 and 17.7 wt% (average = 14.4 wt%). They have lower A/CNK values of 0.85–1.02, making them to classify as metaluminous (Fig. 5b) and have narrow range of Fe# between 0.72 and 0.81 and low Mg# varying from 17 to 42; they are plotted on the field of magnesian rocks according to Fe# versus  $SiO_2$  diagram, while granoporphyries are on the ferroan rocks (Fig. 5c). They have high  $K_2O$  content (2.35–5.37 wt%), indicating their high-K calc-alkaline granitoids feature (Fig. 5d). Metagranitoids contain  $MgO$  (0.25–2.79 wt%),  $FeO^T$  (1.01–6.62 wt%),  $MnO$  (0.03–0.12 wt%), high Sr (195–701 µg/g), and low Cr (20 µg/g). On major element variation diagrams, metagranitoids exhibit negative correlation relationships between  $SiO_2$  and  $TiO_2$ ,  $Al_2O_3$ ,  $MgO$ ,  $CaO$ , and  $P_2O_5$  (Fig. 6).

High-K calc-alkaline metagranitoids are characterized by a slight enrichment in LREE, depletion in HREE ( $[La/Yb]_{CN} = 4.67\text{--}33.7$  (despite samples KWB052b–68; KRD063–4.6;  $[La/Sm]_{CN} = 2.05\text{--}7.63$ ) on CI-chondrite-normalized REE diagrams (Fig. 7a). They exhibit weak negative Eu anomalies ( $Eu/Eu^* = 0.01\text{--}0.09$ ). On the primitive-mantle-normalized trace element spider diagram (Fig. 7b), these metagranitoids samples are enriched in elevated concentrations of Rb, Ba, Th and Pb and depletion in Nb, Ta and Ti ( $[Nb/La]_{PM} = 0.07\text{--}0.36$ ), enrichment of the LREE ( $[Th/La]_{PM} = 0.7\text{--}4.2$ ) in respect to the adjacent elements. These patterns also observed in the calc-alkaline metagranitoids. According to the discrimination diagrams by Pearce et al. (1984), all samples are classified into the volcanic arc granite (Fig. 8a, b). On the trace element tectonomagmatic plots for I-type rocks, which discriminates between slab failure and arc rocks, metagranitoids mostly belong to slab failure field on La/Sm versus Sm/Yb, La/Yb versus Gd/Yb, La/Yb versus Ta + Yb, Ta/Yb versus Ta + Yb, Gd/Yb versus Nb + Y and Sm/Yb versus Nb + Y diagrams (Fig. 9).

#### 4.3. Zircon U-Pb geochronology

Analytical results are presented in Supplementary data 1, representative zircon CL images are given in Fig. 10 and concordia plots of the data are presented in Fig. 11. The obtained ages are shown in a decreasing order.

Sample KRD063 has zircons that are colorless or light brown, mostly subhedral, stubby, up to 200 µm in length (Fig. 10a). These zircons display weak oscillatory zoning or without zoning in CL image. The measured Th/U ratios ranging from 0.04 to 1.03. Five zircons possess Th/U ratios lower than 0.1 (Fig. 12a) with concordia age of  $570 \pm 5.7$  Ma (MSWD = 3.8; Fig. 11a), and one zircon  $1914.2 \pm 19$  Ma, to be considered to represent the inherited zircon age of the metagranite.

Sample KWB052 is a metagranite with colorless or light brown zircons and euhedral to anhedral shapes, about 100–200 µm in size, aspect ratios from 1 to 3, some zircons manifest patchy zoning or homogeneous core surrounded by bright rims in CL images (Fig. 10b). Patchy zoning may reflect the strain experienced by zircon during final magmatic emplacement (Paquette et al., 1995). From sixteen analyses, which Th/U ratios ranging from 0.02 to 2.1, two of them yielded concordia age of  $565 \pm 7.7$  Ma (Fig. 11b). Zircons with low Th/U concordia age reflects the metamorphic event (Fig. 12a, b).

Sample KRD056 is characterized by small (~150 µm), subhedral to anhedral brown or light brown zircons. Grains show moderate CL-response with oscillatory zoning (Fig. 10c). Th/U ratio varies between 0.9 and 2.2. Twenty-seven discordant zircons described common concordia age of  $1889.9 \pm 4$  Ma (MSWD = 0.012; Fig. 11c), which reflects the crystallization age of volcanics.

Sample KWB048 has clear prismatic euhedral and subhedral zircons up to 300 µm, whose aspect ratios are from 1 to 3 (Fig. 10d). Many zircons have bright CL core and distinct oscillatory zoning, some zircons have thin bright rims. Seventeen analyses provide a concordia age of  $1880 \pm 4.6$  Ma (MSWD = 1.7; Fig. 11d), measured Th/U ranging from

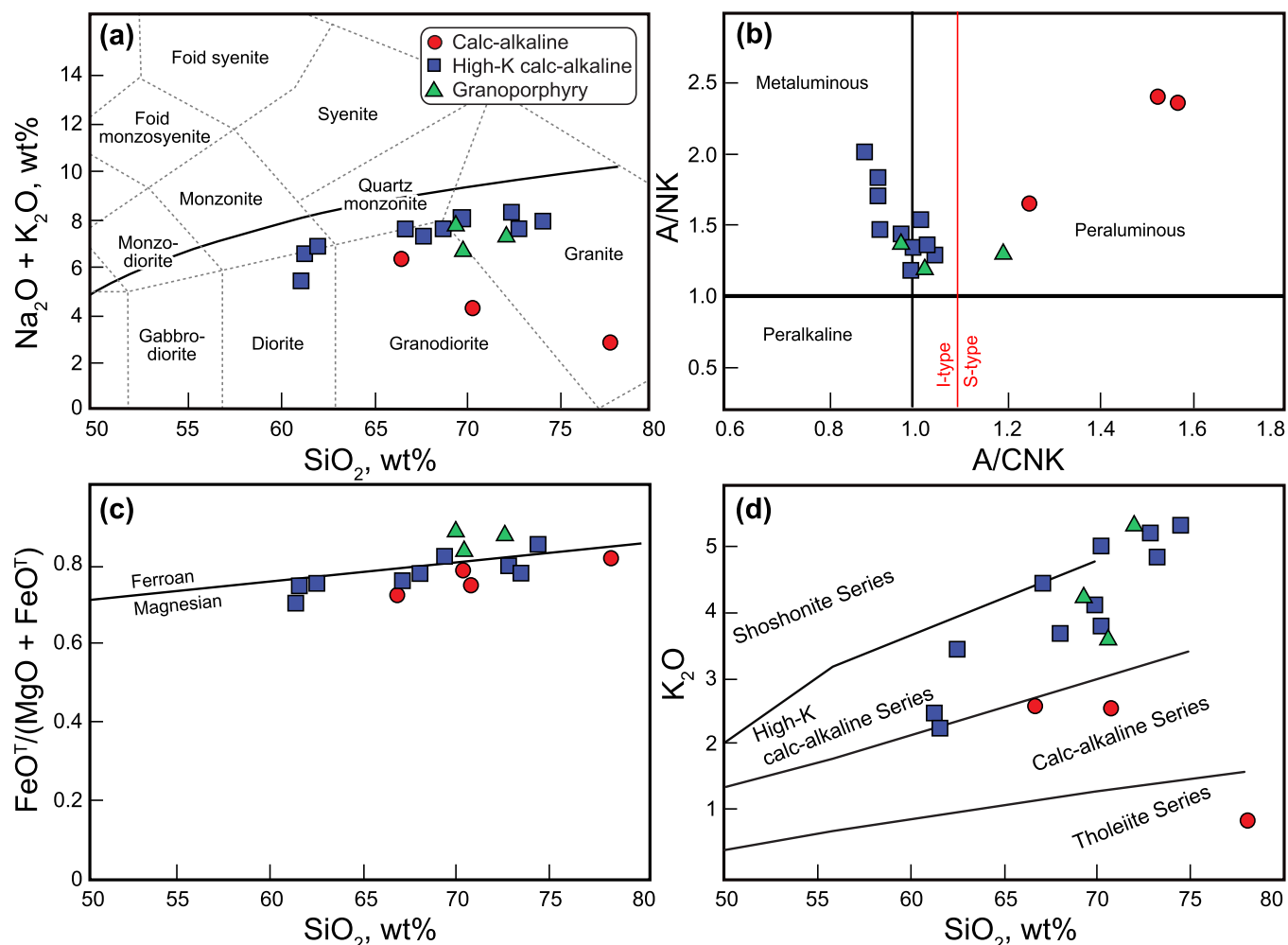


**Fig. 5.** Major element discrimination diagrams showing the compositions and characteristics of the studied metagranitoids and granoporphyries (a)  $\text{SiO}_2$  versus  $(\text{Na}_2\text{O} + \text{K}_2\text{O})$  total alkali-silica (TAS) diagram (after Irvine and Baragar, 1971), (b)  $\text{A/CNK}$  versus  $\text{A/NK}$  diagram, boundary line is from Maniar and Piccoli (1989), (c)  $\text{FeOT}/(\text{MgO} + \text{FeOT})$  wt% versus  $\text{SiO}_2$  plot (after Frost et al., 2001), (d)  $\text{K}_2\text{O}$  wt% versus  $\text{SiO}_2$  wt% plot (Peccerillo and Taylor, 1976).

1.2 to 2.6. The concordia age is interpreted as the crystallization age of the metamonozigranite.

Sample KWB053 contained colorless zircons euhedral to subhedral, no longer than 200  $\mu\text{m}$  in length, stubby, with aspect ratios 2 or less, zircons exhibit fine-scaled oscillatory zoning in CL-image (Fig. 10e). Twenty-seven zircons were analyzed, and their Th/U ratios ranging from 0.89 to 2.6. All analyzes are plotted on concordia diagram, providing common concordia age of  $1876.4 \pm 7.8$  Ma (MSWD = 0.88; Fig. 11e). We interpreted this age as crystallization age of the metagranodiorite.

Sample KYB065 contained transparent to light brown zircons, up to 200  $\mu\text{m}$  in length, varies from stubby to elongated in shape, with aspect ratios from 1 to 3. In CL images, zircons show wide oscillatory zoning, some zircons have homogeneous xenocrystic core (Fig. 10f). Thirty-six grains were chosen to analyze. The measured Th/U ratios ranging from 0.6 to 2.1. All zircons are plotted on or close to the concordia, describing concordia age of  $1874.5 \pm 3.9$  Ma (MSWD = 0.68; Fig. 11f), interpreted to be the metagranite crystallization age.

Sample KWB049 contained transparent to light brown zircons, up to 150  $\mu\text{m}$  in length, mostly stubby with aspect ratios not exceeding 2, prismatic euhedral in shape. In CL images, zircons show narrow oscillatory zoning, but some zircons contain xenocrystic core (Fig. 10g). Thirty zircons were chosen to analyze. The measured Th/U ratios are ranging from 0.9 to 1.9. All zircons are plotted close or on the concordia,

describing common concordia age of  $1859.6 \pm 9.6$  Ma (MSWD = 0.88; Fig. 11g), interpreted to be the time of crystallization of the metamonozodiorite.

Sample KRD060 has stubby to slightly elongate, euhedral to subhedral, clear zircons with lengths up to 200  $\mu\text{m}$  and aspect ratio about 1.5. Many zircons have CL-bright zones in xenocrystic core with faint oscillatory rims (Fig. 10h). The Th/U varies range from 0.7 to 2.3. Concordia age of ten grains yielded  $1858.5 \pm 15$  Ma (MSWD = 1.9, Fig. 11h), which is interpreted as the crystallization age of metamonozigranite.

Sample KRD062 has brown but mostly clear, euhedral or subhedral stubby and rounded zircons 100–150  $\mu\text{m}$  in length. Twenty-four grains were selected to be analyzed for this sample (Fig. 10i). Th/U ratios range from 0.99 to 2.5. All analyzes are plotted on or very close to the concordia, yielding concordia age of  $1854.7 \pm 9.7$  Ma (MSWD = 2.6; Fig. 11i), which is considered as crystallization age of the metagranodiorite.

#### 4.4. Apatite U-Pb geochronology

Two samples, from the Southern Ufipa Terrane and the Kate-Ufipa Complex (KYB065 and KRD062) out of 9 samples, yielded successfully apatite U-Pb ages due to their high enough concentration of U and Pb. The separated apatite grains are colorless, euhedral to subhedral, 100–

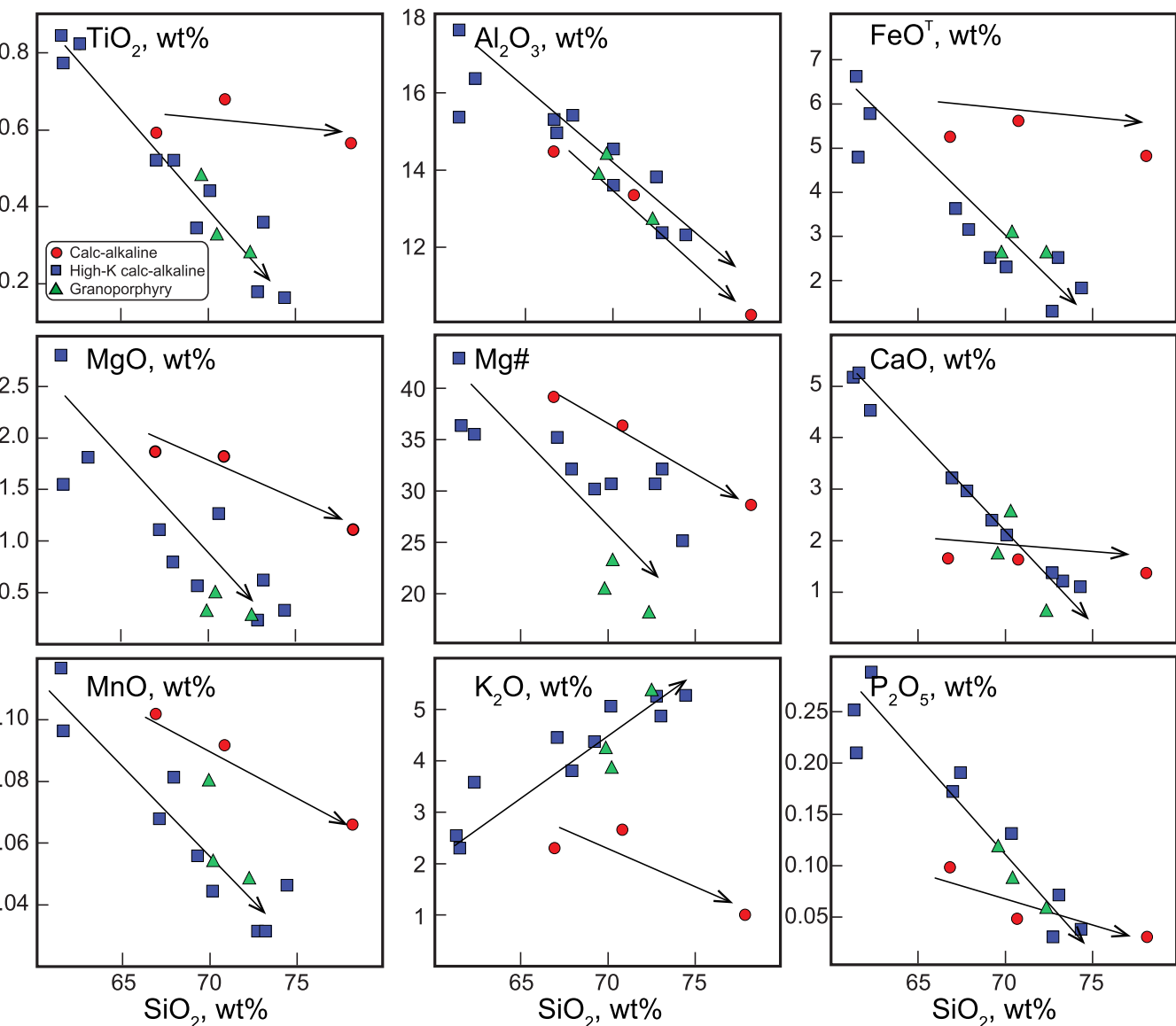


**Fig. 6.** Harker diagrams showing the magmatic evolution of the studied metagranitoids and granoporphries.

200 µm in length, homogeneous with no obvious zoning, partially enclosed in the major primary minerals. Results of analysis are presented in Supplementary data 2 and concordia plots of the data are presented in Fig. 13. Eight spots of sample KYB065 define an isochron line with an intercept age of 1878 ± 55.9 Ma on a Tera-Wasserburg plot (Fig. 13a). Eleven spots of sample KRD062 build an isochron line with age of 1864 ± 79.9 Ma (Fig. 13b). Those apatite ages overlap of zircon U-Pb ages of the same samples. U-Pb analyses of apatite exhibit a broad discordia array that scatters and initial  $^{207}\text{Pb}/^{206}\text{Pb}$  ratio varying between 0.721 and 0.757.

## 5. Discussion

### 5.1. Geochemical constraints for Paleoproterozoic convergent margin

The whole-rock major element compositions show that the weakly foliated Kate-Ufipa Complex associated with granoporphries from the Bangweulu Block and metagranitoids from the Northern Ufipa Terrane, share similar geochemical features, in spite of the net boundary of the Bangweulu Block and the Ufipa Terrane demarcated by shear zones

(e.g. De Waele et al., 2006b). Major element variation is consistent with the subdivision of Boniface and Appel (2018), differing between the North and the South Ufipa Terranes. Although calc-alkaline metagranitoids from the South Ufipa Terrane exhibit different major element characteristics, their trace element and REE compositional trend is similar (Table 2; Fig. 7). The geochemical resemblance among metagranitoids including granoporphries implies that these rocks were formed under similar igneous processes in akin tectonic settings.

Granitoids including intermediate rocks may form in various ways, such as the (1) fractional crystallization of underplated basaltic magmas (Grove and Brown, 2018), (2) mixing of crustal derived silicic and mantle-derived mafic magmas (e.g. Guo et al., 2012), (3) partial melting of the lower crust (Bryan et al., 2008), and (4) water-induced melting of the mantle wedge metasomatized by subduction derived fluids or melts (e.g. Hawkesworth and Kemp, 2006). Melting by fractional crystallization or partial melting generates systematic trends between SiO<sub>2</sub> and other major elements (e.g. Xu et al., 2009). Such trends are shown by high-K calc-alkaline samples (Fig. 6). Fractionation of clinopyroxene and hornblende causes decreases in MgO, FeO, and CaO with increasing SiO<sub>2</sub>. Decreases in Al<sub>2</sub>O<sub>3</sub> and Sr concentrations with increasing SiO<sub>2</sub> are

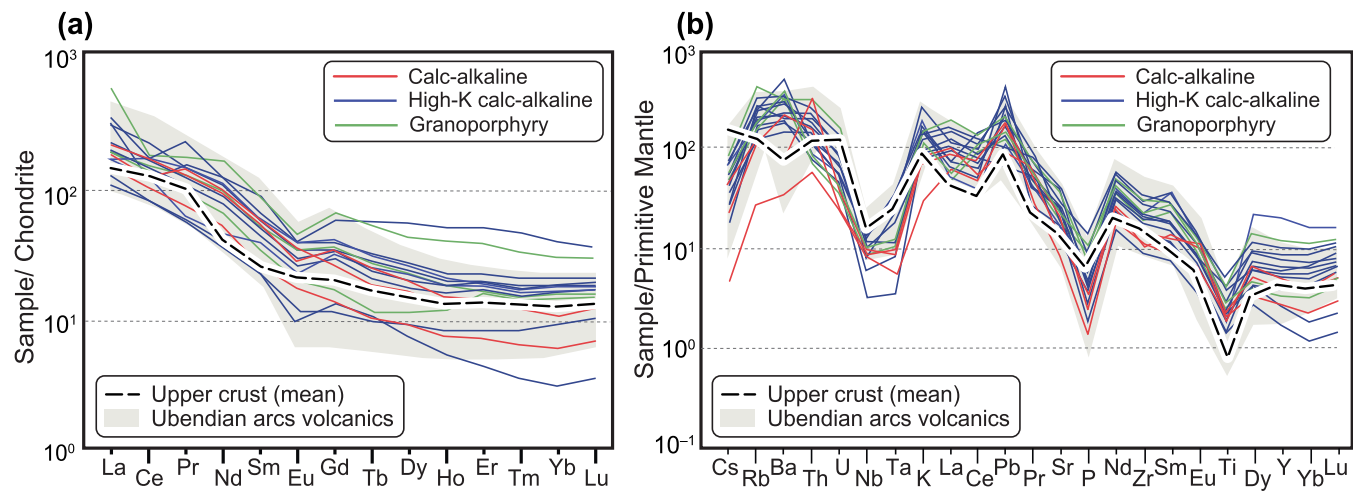


**Fig. 7.** (a) Chondrite-normalized REE patterns and (b) primitive-mantle-normalized trace element spidergrams for the studied metagranitoids of the Ufipa Terrane, Paleoproterozoic Ubendian Belt. Both of chondrite and primitive-mantle values are from Sun and McDonough (1989). The grey shaded areas indicate geochemical patterns of Paleoproterozoic granitoids and metavolcanics from western Ubendian Belt adopted from Kazimoto et al. (2014a, 2014b) and Tulibonywa et al. (2017) respectively. The reference geochemical patterns of continental arc magmas. The comparison data of Upper Continental Crust is from Rudnick and Gao (2005).

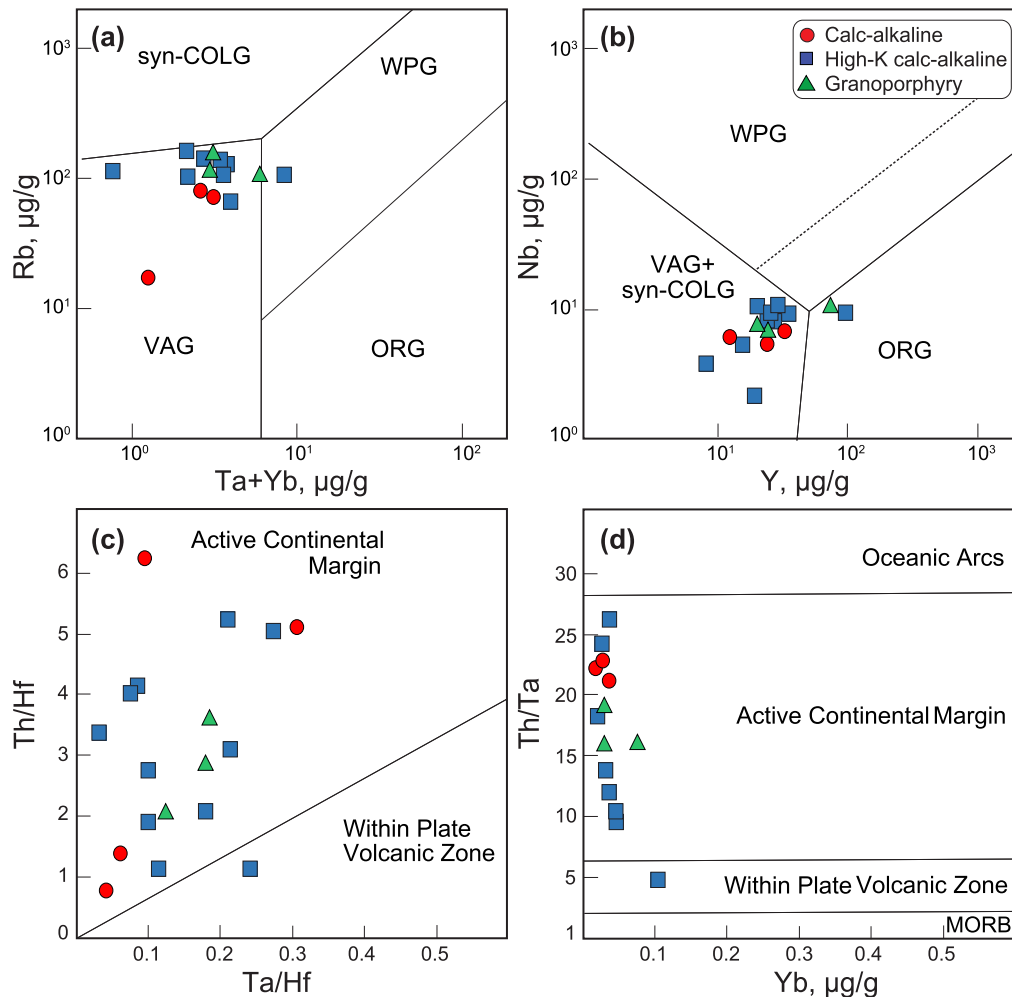


**Fig. 8.** Tectonic discrimination diagrams for the studied samples: (a) Rb versus Ta + Yb; (b) Nb versus Y (Pearce et al., 1984); (c) Ta/Hf versus Th/Hf and (d) Yb versus Th/Ta (Schandl and Gorton, 2002). See details in text.

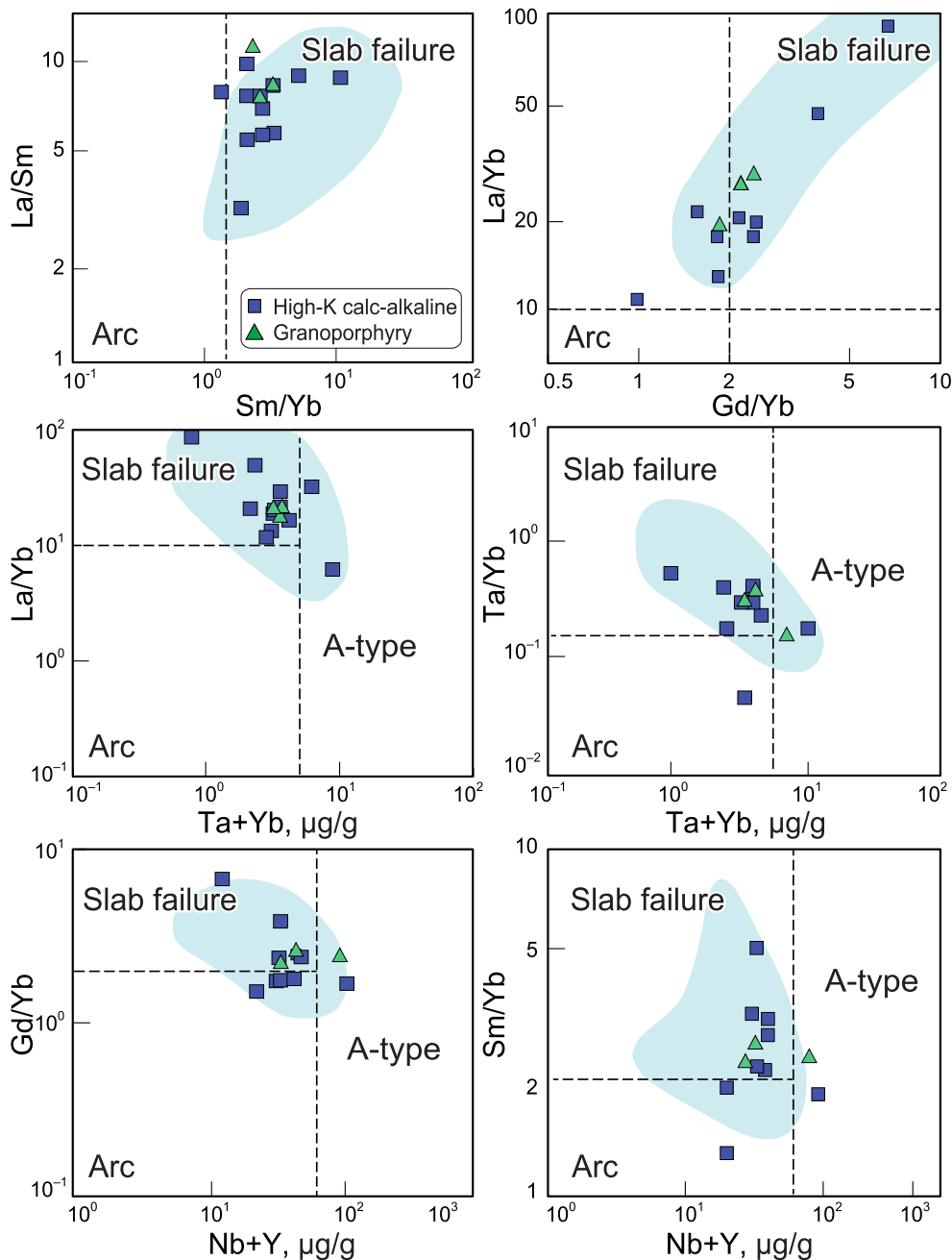


**Fig. 9.** Geochemical comparisons with arc granitoids, slab-failure-related granitoids, and A-type granitoids; the lines (dashed lines) divided each compositional field are referred to (Whalen and Hildebrand, 2019): La/Sm versus Sm/Yb, La/Yb versus Gd/Yb, La/Yb versus Ta + Yb, Ta/Yb versus Ta + Yb, Gd/Yb versus Nb + Y, Sm/Yb versus Nb + Y (Hildebrand and Whalen, 2019). Coordinates for plot fields are based on these values: Nb/Y (0.4), Gd/Yb (2.0), Sm/Yb (2.5), Gd/Yb (2.0), La/Yb (10), Ta/Yb (0.3) and Nb + Y (60). Colored areas represent compositional fields of granitic gneisses and granites from the Ubendian Belt (De Waele et al., 2006a; Kazimoto et al., 2014a, 2014b; Tulibonywa et al., 2017).

correlated with the fractionation of plagioclase, and decreases in  $\text{P}_2\text{O}_5$  and  $\text{TiO}_2$  may reflect the fractionation of accessory minerals such as apatites and rutiles. However, if metagranitoids were formed by fractional crystallization of basaltic or andesitic magmas, then the volume of basaltic or andesitic rocks exposed in the study area should greatly exceed that of the granitoids. This is not the case, and voluminous metagranitoids and granoporphryies are exposed in our study area. In addition, a mixing model for mantle-derived mafic melt and crustal derived silicic magma is not suitable for the petrogenesis of studied samples. In such case, mixing process would cause a decrease in the silica content of the rocks and enrichment in Cr, Co, and Ni, presence of MME (mafic magma enclaves), which is not observed (Cantagrel et al., 1984).

High-K calc-alkaline samples, have ASI (aluminum saturation index) content 0.85–1.23, combined with the presence of titanite and hornblende indicates that these granitoids are I-type. In contrast to high-K calc-alkaline samples, calc-alkalines are richer in  $\text{MgO}$ ,  $\text{FeO}$ ,  $\text{Ni}$ ,  $\text{Cr}$ ,  $\text{TiO}_2$ ,  $\text{CaO}$ , and  $\text{MnO}$  and show irregular trend on Harker diagram (Fig. 6). Also, they exhibit high ASI (1.26–1.53) and, indicating their S-type characteristic (Chappell and White, 2001). Calc-alkaline, peraluminous metagranitoids and evolved rocks could have resulted by the fractionation of plagioclase and hornblende during the evolution (Zen, 1986). Their evolved nature characterized by their low Mg#, and low Cr, Co, and Ni contents (Table 2), and indicate that these granites and volcanic rocks were chemically fractionated relative to the mantle. Incompatible

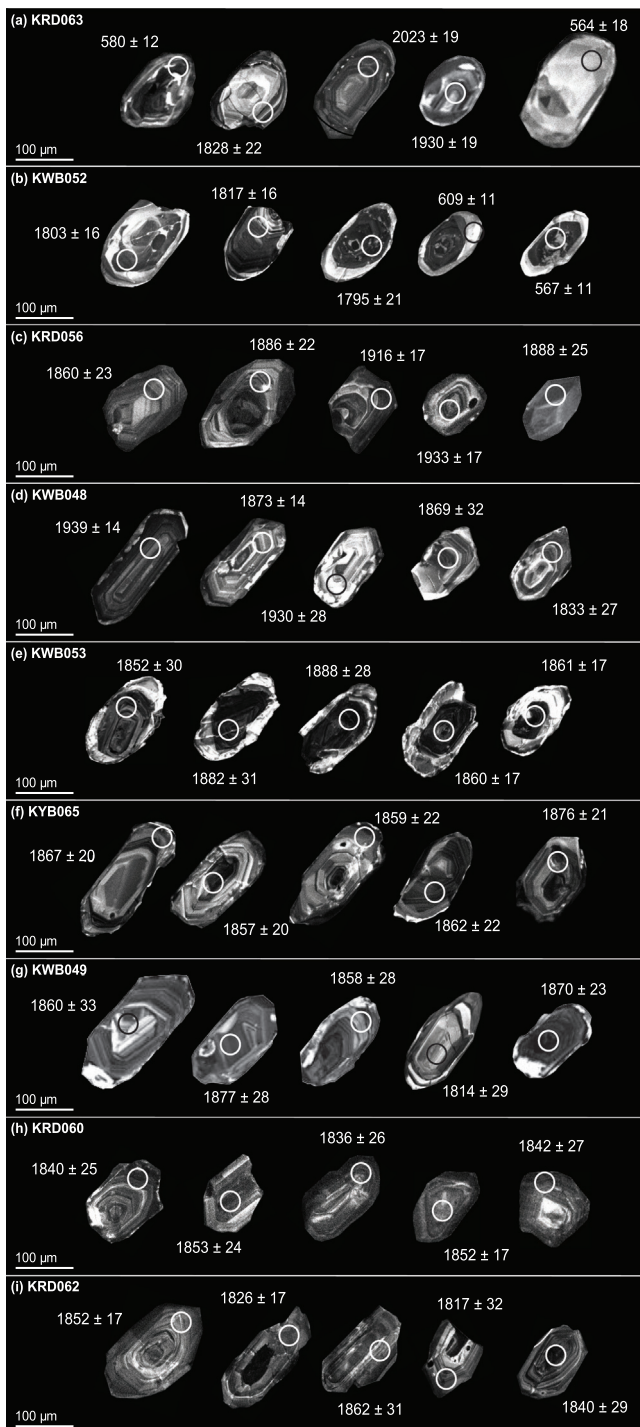


**Fig. 10.** Cathodoluminescence (CL) images of representative zircon crystals from the studied metagranitoids and granoporphries, with corresponding Pb-Pb ages.

element ratios remain unchanged even during partial melting and/or crystal fractionation events, which made them useful to constrain primary magmatic features (Pearce and Peate, 1995; Polat and Hofmann, 2003).

Trace element characteristics such as high Zr/Nb ratio (aveage = 26), Th/Nb ratio (average = 1.9), Hf/Ta ratio (average = 10.7) and depletion of Ti-Nb-Ta are typical of arc magma, which originate as a result of partial melting of the upper mantle (Gill, 2011; Pearce and Peate, 1995). Metagranitoids and granoporphries have high SiO<sub>2</sub>, but low

MgO, FeO<sup>T</sup>, CaO, Sc, Cr, Co, and Ni contents. Their LREE and LILE enrichments coupled with HFSE depletions and wide range of HREE concentrations (Fig. 7a, b). This composition suggests involvement of crust and heterogeneous source possibly indicating derivation from the partial melting of the lower continental crust, subducting slab and the upper mantle. On widely using geodynamic discrimination diagram for granites, invented by Pearce et al. (1984) which use elements such as Rb, Nb, Y, Yb and Ta (Fig. 8a, b), the calc-alkaline metagranitoids are mostly plotted on VAG (Volcanic Arc Granites), whereas two samples are plotted on WPG (Within Plate Granite) field. On another trace element diagrams of Th/Hf versus Ta/Hf and Th/Ta versus Yb (Fig. 8c, d), the rocks belong to the active continental margin field.

Recent studies recognized that magmatism formed in slab failure setting could be masked and misinterpreted as an arc (Hildebrand and Whalen, 2014, 2017; Hildebrand et al., 2018). Because of the buoyancy difference between oceanic and continental crust, it is expected some sort of slab break-off after every closure of an oceanic basin. Therefore, slab failure is the rupture and separation of subducting plates and an integral phenomenon of the plate tectonic and a natural consequence of subduction (e.g. Atherton and Ghani, 2002; Davies, 2002). Slab failure rocks originated from the deep mantle processes that likely include partial melting of the mafic upper portion of the torn slab, leaving a garnet-bearing, plagioclase-free eclogitic residue (Hildebrand and Whalen, 2017). Due to their location and short-lived, generally voluminous character, slab break-off magmatism is usually confused in magmatic arc activity. The depth of break-off largely controls the volume of magmatism and associated metamorphism of the orogen. The rebound of the partially subducted continent will cause intense uplift and exhumation of deeper crustal levels (Duretz et al., 2011; Duretz and Gerya, 2013). Break-off occurring in shallow depths creates narrow orogens, lower-grade metamorphism, and intense rates of exhumation. In contrast, deep break-off creates broad orogens with higher grade metamorphism and more subdued rebound and exhumation (Duretz et al., 2011). In this case, the resultant uplift and exhumation might cause the erosion of the arc in the overriding plate, leaving only minor vestiges of the upper crust (Hildebrand and Whalen, 2014). Whalen and Hildebrand (2019) developed new approaches to discriminate different arc magmatism by using the differences in trace element concentrations of large number of well-studied samples. Their new trace element tectonomagmatic plots for I-type rocks (restricted for S- and A-types) discriminates between slab failure and arc rocks. They tested empirically the diagrams, observing the distinction of trace elements such as Sr/Y, Nb/Y, Gd/Yb and La/Yb to arrive at separative values (Fig. 9). The strong partitioning of HREE into residual garnet and absence of Sr-plus Eu-hosting plagioclase in slab failure magmatism, exhibit a distinctive high La/Yb, Gd/Yb, Sm/Yb and Sr/Y ratios. Instability of a Ti-rich phase such as rutile, plus residual garnet, produce their high Nb/Y and Ta/Yb ratios. High Sm/Yb in slab failure magmatism reflects their greater depth of melting (Putirka, 1999).

On the newly developed diagrams, metagranitoids mostly belong to slab failure field on La/Sm versus Sm/Yb, La/Yb versus Gd/Yb, La/Yb versus Ta + Yb, Ta/Yb versus Ta + Yb, Gd/Yb versus Nb + Y and Sm/Yb versus Nb + Y (Fig. 9). Predominance of felsic over mafic magma composition; the diverse signatures of granites (e.g. volcanic-arc granite, within-plate granite); and heterogeneity of origin can be interpreted by slab failure setting (Massawe and Lentz, 2020; van Staal et al., 2009). Presence of Paleoproterozoic high-pressure metamorphic rocks in the Ufipa Terrane suggest that slab failure occurred at a great depth (Hildebrand and Whalen, 2014) and it can explain the absence of "real" arc magmatism along the Bangweulu Block and the Ufipa Terrane.

## 5.2. Geochronological constraints on magmatism

Zircons with high Th/U ratios (> 0.2) are of magmatic origin, whereas those having a low Th/U ratio (< 0.1) have undergone a secondary process such as metamorphism and hydrothermal alteration

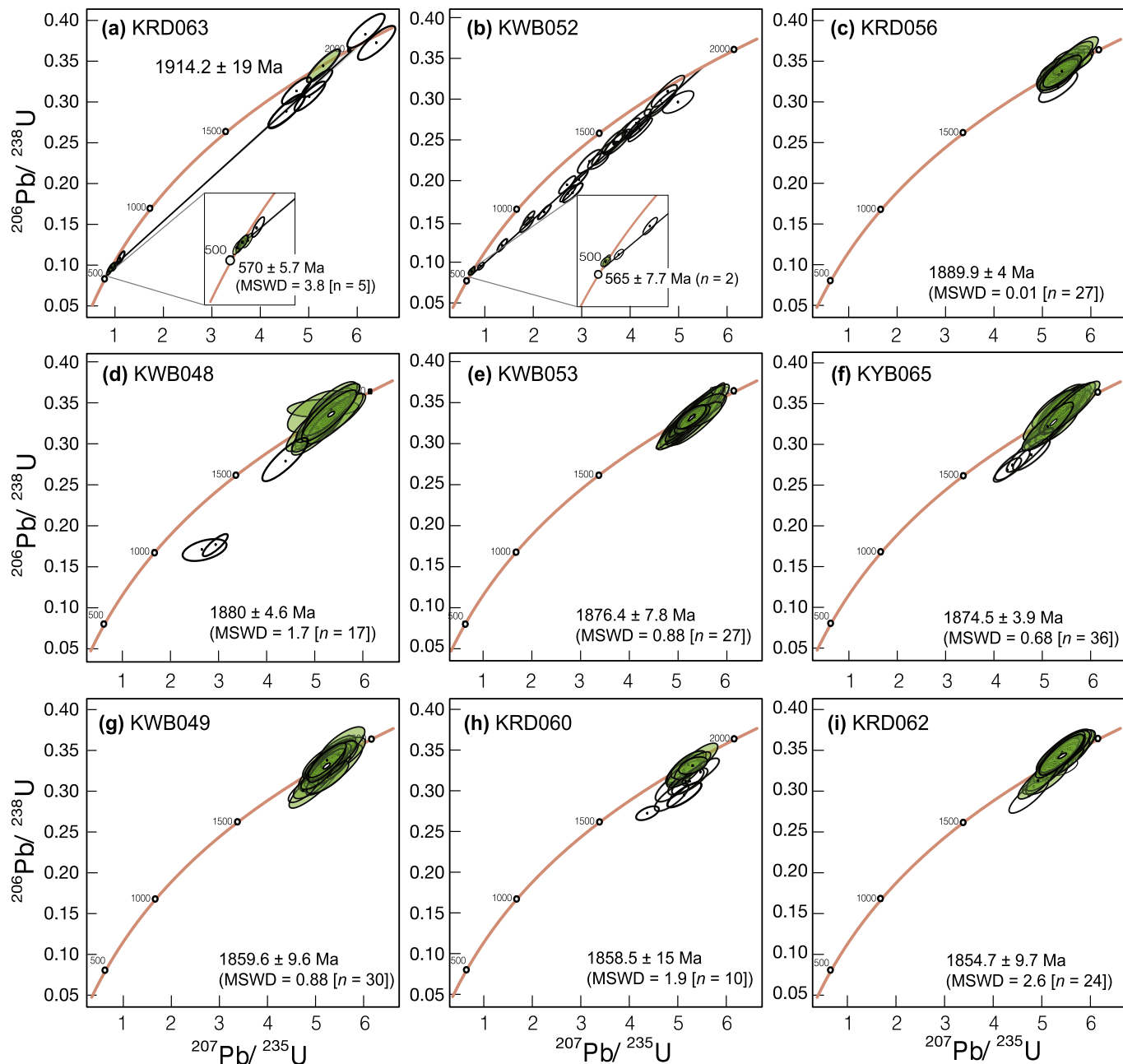
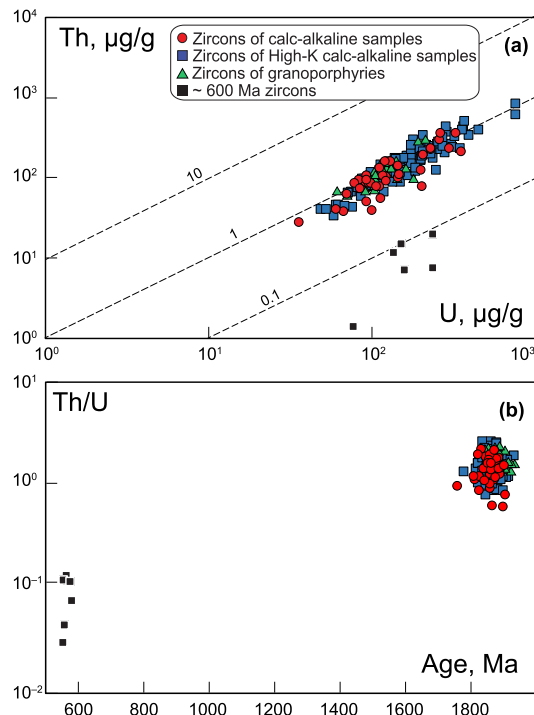


Fig. 11. U-Pb concordia diagrams of zircons from the metagranitoids and granoporphries, showing U-Pb isotope ratios. White spots indicating not calculated spots.

(e.g. Hartmann et al., 2000). High Th/U ratios ( $> 0.15$ ) have also been recorded in recrystallized zircon, and these zircons are grown during high-temperature metamorphism (e.g. Yakymchuk et al., 2018). The dated zircons with high Th/U ratios and clear oscillatory zoning (Fig. 12a) are most likely to be magmatic origin (Pidgeon, 1992).

Zircon LA-ICPMS U-Pb data from the metagranitoids and granoporphries on the boundary of the Bangweulu Block and the Ufipa Terrane of the Ubendian Belt show concordia ages at  $1889.9 \pm 4$ ,  $1880.5 \pm 4.6$ ,  $1876.4 \pm 7.8$ ,  $1874.5 \pm 3.9$ ,  $1859.6 \pm 9.6$ ,  $1858.5 \pm 15$  and  $1854.3 \pm 9.7$  Ma and emplaced during a time period about 40 Myr. Ages show no systematic younging along the studied area, suggesting geochronological similarity along the Bangweulu Block boundary and the Ufipa Terrane. These ages support the limited ages by the pioneering works of Schandlmeier (1983), who reported Rb-Sr isochron age for granite of the Ufipa Terrane ( $1838 \pm 86$  Ma), and TIMS

U-Pb zircon age ( $1864 \pm 32$  Ma) (Fig. 14a) by Lenoir et al. (1994). Ages of the Ufipa metagranitoids are in good correlation with magmatic ages of different terranes of the Ubendian Belt (Fig. 14b), and a metamorphic age of granulite-facies monazite and zircon from metapelites in the Ufipa Terrane. We attribute this high-grade metamorphism to the heat advection by high-K and calc-alkaline magmas into a continental margin. This scenario has also been applied to the Paleoproterozoic granulites of the Katuma Terrane (Kazimoto et al., 2015). Extensive volcano-plutonic rock ages in the margins of the Bangweulu Block (Fig. 14c; De Waele et al., 2006b). For example, the felsic to mafic lavas extruded in the Irumide Belt during 1.88–1.85 Ga. Similarly, at the Mansa area, southwestern margin of Bangweulu Block, granitoids and felsic lavas are emplaced at 1.89–1.86 Ga (De Waele and Fitzsimons, 2007). Our datasets are also consistent with a 1.89–1.86 Ga subduction event within the Usagaran Belt, which is also supported by arc



**Fig. 12.** (a) Th versus U diagram for magmatic and metamorphic zircons. (b) U-Pb age versus Th/U of the analyzed zircons from metagranitoids and granoporphryie.

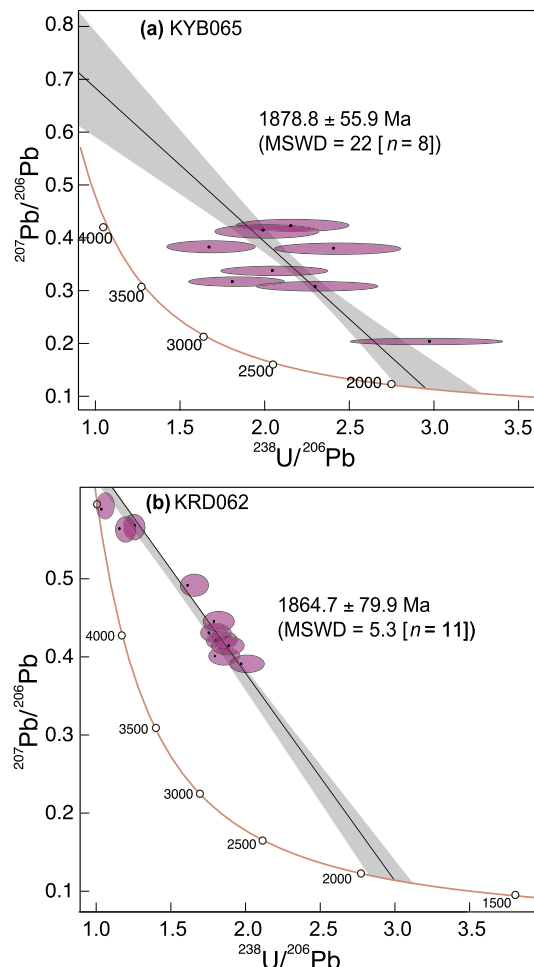


**Fig. 13.** Tera-Wasserburg concordia diagrams for discordant lines and intercept ages data of apatites from metagranitoids, showing U-Pb isotope ratios.

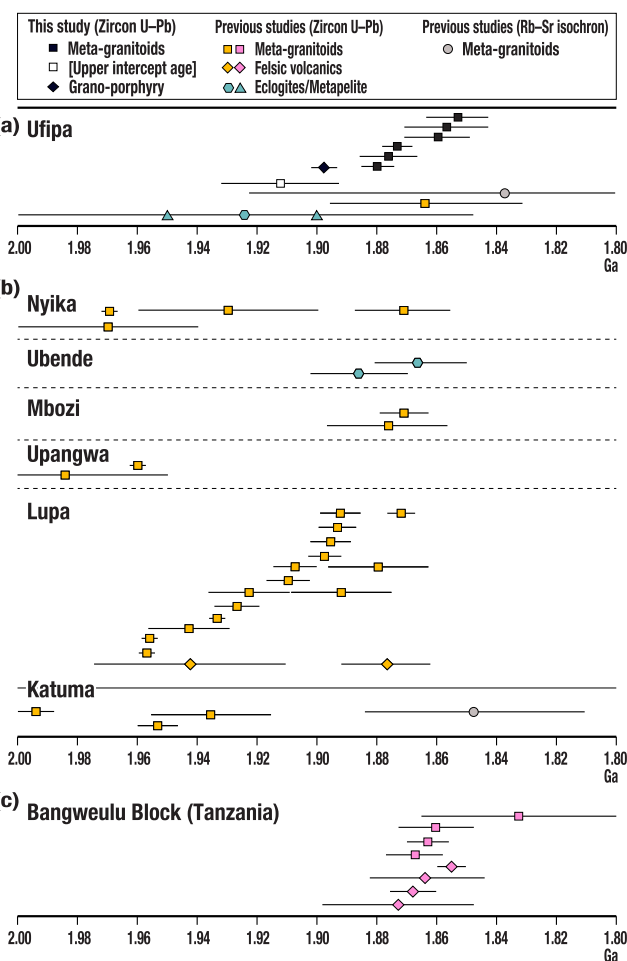


**Fig. 14.** Summary of geochronological data obtained in this study in relation to previous U-Pb and Rb-Sr magmatic ages of igneous rocks for (a) the Ufipa Terrane, (b) different terranes of the Ubendian Belt, and (c) the Bangweulu Block (for reference see Fig. 2). Eclogite ages are also shown to coincide with the subduction magmatism of the Ubendian Belt.

magmatism (Fig. 15), high-pressure, low-temperature metamorphism, crustal thickening and gold mineralization (e.g. Manya and Maboko, 2016).

### 5.3. Geochronological constraints on metamorphism

The mineral assemblage, gneissic texture and banding of the studied metagranitoids imply that our study area experienced low to intermediate metamorphic conditions after their magmatic emplacement. Particularly, samples KWB049 and KYB065 contained sodic plagioclase, hornblende, epidote, garnet and kyanite. It suggests that metamorphism

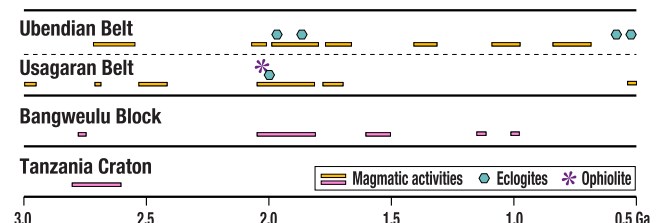


**Fig. 15.** Summary of magmatic activity, ophiolite and eclogite-formations for the Precambrian context of the Ubendian–Usagaran Belt, the Bangweulu Block and the Tanzania Craton.

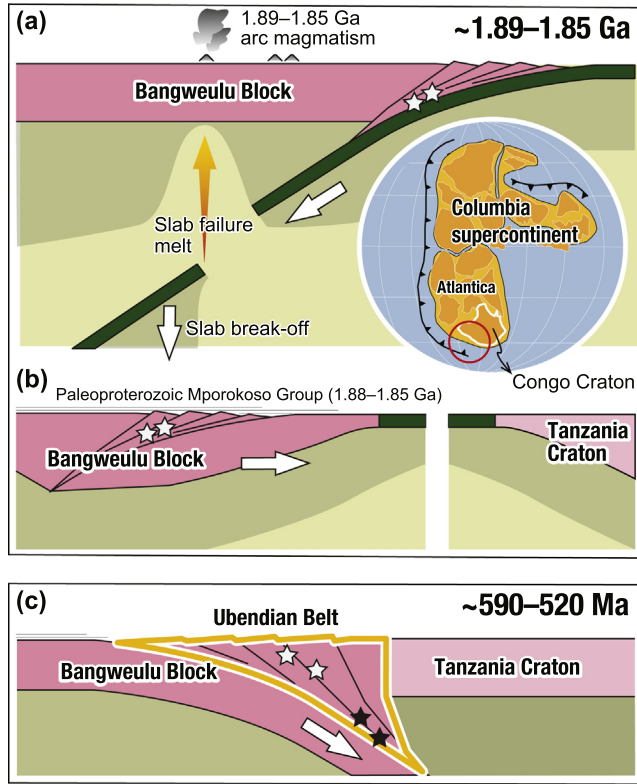


**Fig. 16.** Tectonic model of metagranitoids and granoporphries emplacement of the Ufipa Terrane. (a) Cross-section depicting a slab-failure magmatism by the oceanic subduction of the Ufipa Terrane beneath the Bangweulu Block. Location of the Congo Craton (present-day Central African Shield) during the Columbia Supercontinent assembly (Grenholm, 2019) is also shown. (b) Deposition of volcanicogenic sediments of the Mporokoso Group on the Bangweulu Block; (c) Neoproterozoic collision of the Bangweulu Block beneath the Tanzania Craton during the consolidation of the Central African Shield (Congo Craton) by the Pan-African orogeny, amalgamation of the Gondwana Supercontinent.

occurred under epidote-amphibolite to amphibolite facies conditions. Lack of metamorphic zircon or overgrowth rim hampered the dating of metamorphic events for these samples.

Seven zircons of two metagranitoids from the Northern Ufipa Terrane have low Th/U ratios, similar to the metamorphic zircons (Fig. 12a), suggesting tectonothermal overprints of Neoproterozoic collisional metamorphism at  $570.4 \pm 5.7$  and  $565 \pm 7.7$  Ma (Fig. 12b). Our data coincide with the previous findings. Several parts of the Ubendian Belt were re-worked during 590–500 Ma. U-Pb SHRIMP zircon ages of  $593 \pm 20$ ,  $548 \pm 39$ , and  $524 \pm 12$  Ma are obtained from kyanite-free eclogites in the Northern Ufipa Terrane (Fig. 15; Boniface et al., 2012; Boniface and Schenk, 2012).

Apatite is widely used for constraining time-temperature information on low temperature processes because of their comparably low closure temperature of  $375\text{--}600^\circ\text{C}$  (Cochrane et al., 2014; Kirkland et al., 2018). Apatite ages of samples from the Kate-Ufipa Complex and the Southern Ufipa Terrane (Fig. 2) yielded discordia lines with intercept ages between  $1.88 \pm 56$  and  $1.86 \pm 80$  Ga, respectively. Although, uncertainty of apatite ages is large, they are yielded obvious Paleoproterozoic ages, which is within the range of zircon ages. Smaller grain sized apatite ( $100\text{--}200\ \mu\text{m}$ ) in our samples probably constrain younger age of magmatic component given Pb-in-apatite diffusion an spherical geometry characteristics (Cherniak, 2005). Apatite typically incorporates substantial amounts of common Pb compared to U (i.e. low  $^{238}\text{U}/^{204}\text{Pb}$ ) when it crystallizes (Chew and Spikings, 2015; Kirkland et al., 2017). This results in a slow increase with time in the ratio of radiogenic Pb to non-radiogenic Pb (e.g.  $^{206}\text{Pb}$  radiogenic/ $^{206}\text{Pb}$  initial). High common Pb content in the analyzed apatite array may

imply interaction with a distinct, more radiogenic crustal source (Fig. 13). The grain shapes and textural relationships of apatite are indicative of a primary magmatic origin and its U-Pb age is interpreted as the time of last resetting during a thermal event at  $\sim 1.86$  Ga. All apatite samples yield similar high upper intercepts with  $^{207}\text{Pb}/^{206}\text{Pb}$  ratios comparable to 1.9–1.8 Ga common Pb of the Pb evolution model by Stacey and Kramers (1975), implying the incorporation of Pb into the crystal structure from the magmatic environment during apatite crystallization. Paleoproterozoic apatites were only confirmed from the Southern Ufipa Terrane and the Kate-Ufipa Complex. These suggest that the Pan-African overprint effect was not equal throughout the Ufipa Terrane. Neoproterozoic tectonothermal events was not intense enough to anneal apatites in the Southern Ufipa Terrane and the Kate-Ufipa Complex. In contrast, the Neoproterozoic overprint was severe to reset zircon U-Pb age in the Northern Ufipa Terrane.

#### 5.4. Geodynamic setting and implications for the Central African Shield amalgamation

The Paleoproterozoic geodynamic evolution of the Ubendian Belt is dominated by an active continental margin followed by collision (e.g. Boniface and Tsujimori, 2021). Metagranitoids from the Ufipa Terrane of the Ubendian Belt and northeastern portion of the Bangweulu Block emplaced between 1.89 and 1.85 Ga show silimar trace element pattern. They are formed by break-off of the subducting oceanic slab. Slab failure magmatism is possibly generated by melting of a torn subducting slab and the upper mantle above the subducting oceanic crust. It is followed by ascent and evolution of these magmas at the interface of the upper mantle and lower crust, which lead to partial melting of lower crust. While ascending, the magmas differentiated and mixed with the crustal magmas, resulting in the development of 1.89–1.85 Ga calc-alkaline magmas of the Ufipa Terrane and the northeastern Bangweulu Block (Fig. 16a). Consequently, the Mporokoso Group sediments are deposited from volcanic and plutonic source between 1.88 and 1.85 Ga (Fig. 16b).

Subduction and accretion in the Ubendian Belt to the Tanzania Craton apparently initiated within the Katuma and Lupa Terranes, and proceeded by fusion of the Upangwa and Nyika Terranes as they recorded the oldest magmatism (Fig. 2; Fig. 13b). The activation of subduction culminated between 1.89 and 1.86 Ga, associated with crustal thickening and gold mineralization (Boniface et al., 2012; Kazimoto et al., 2014b; Lawley et al., 2013b, 2014). The subducting oceanic slab formed the Paleoproterozoic 1.89–1.87 Ga eclogites with MORB affinity in the Ubende Terrane is another evidence of the oceanic basin closure. Subsequent collision and accretion between the Tanzania Craton and the Bangweulu Block occurred at  $\sim 1.83\text{--}1.82$  Ga (Boniface et al., 2012). The Ubendian Belt together with the Usagaran Belt evidences an important tectonothermal event: assembly of the Tanzania Craton and the Bangweulu Block with the Congo Craton and forming the Central African Shield as long-lived convergent margin of Archean craton fragments during Paleoproterozoic period (Alessio et al., 2019; Begg et al., 2009) and their participation to the Columbia supercontinent amalgamation.

A different subduction and accretion event in the Ubendian Belt is constrained by 570–565 Ma metamorphic zircon age and eclogite occurrence of the Usagaran Belt. Geochemical compositions indicate that precursors of these eclogites are associated with volcanic rocks of subducted oceanic crust and back-arc basin (Boniface et al., 2012). These volcanic lavas attained their eclogite facies metamorphism after an episodic accretion between the Bangweulu Block and the Tanzania Craton along the Ubendian Belt, commenced at around 590 Ma (Boniface and Schenk, 2012). Closure and accretion were suggested by monazite crystal overgrowth rim of pelitic gneiss, yielding ages between 566 and 556 Ma (Boniface and Appel, 2017, 2018). This period is interpreted as subducting passive margin. The final continent-continent collision is marked by 530 and 520 Ma eclogites (Fig. 16c; Boniface et al., 2012). The 590–520 Ma regional tectonothermal event

of the Ubendian Belt contemporaneous with Neoproterozoic consolidation of the Central African Shield and final Gondwana assembly by the Pan-African orogeny (e.g. Alessio et al., 2019). Eclogite with MORB and back-arc affinity coupled with the Paleoproterozoic active continental margin magmatism of the Ubendian Belt suggest that the Bangweulu Block took a part in the amalgamation of still large Central African Shield as a small separate unit surrounded by ocean during the assembly of the Columbia in Paleoproterozoic and the Gondwana in Neoproterozoic times.

## 6. Conclusions

Metagranitoids, including granoporphyries, from the South and North Ufipa Terranes of the Ubendian Belt and northeastern part of the Bangweulu Block were studied to constrain their geochemical and geochronological features. Based on geochemical, and geochronological data we propose that:

(1) Paleoproterozoic metagranitoids and granoporphyries in the Ufipa Terrane and northeastern portion of the Bangweulu Block cannot be distinguished by geochronology and trace element geochemistry from the each other.

(2) The Ufipa Terrane of the Ubendian Belt has a protolith equivalent to Paleoproterozoic I-type granites. New U-Pb data suggest at least ~40 Myr for the magmatic pulse, between 1.89 and 1.85 Ga.

(3) Geochemical features of metagranitoids such as enrichment in LREE and LILE (e.g. Rb, Ba, Cs, Pb), depletion of HFSE (Ti, Ta, Nb), high La/Yb, Sm/Yb, Gd/Yb and Sr/Y ratios and wide range of HREE interpreted in terms of their formation by melting of the torn slab and upper mantle above the subducting oceanic crust, followed by ascent to the lower crust and subsequent partial melting of lower crust.

(4) Zircons with low Th/U ratio yielded ~570 Ma ages, suggesting a metamorphism during the Pan-African Orogeny in the Northern Ufipa Terrane. The protolith of the Ufipa Terrane is originated from the collided crustal rocks of the Bangweulu Block. Tectonothermal effect of Neoproterozoic collision was unequal throughout the Ufipa Terrane as we found non-annealed Orosirian age apatite in the Southern Ufipa Terrane and the Kate-Ufipa Complex.

(5) The Bangweulu Block and the Ubendian Belt participated in amalgamation of the Central African Shield as separated continents, surrounding oceanic crusts during the Paleoproterozoic Eburnean orogeny and the Neoproterozoic Pan-African orogeny.

Supplementary data to this article can be found online at <https://doi.org/10.1016/j.gr.2020.12.009>.

## Declaration of Competing Interest

None

## Acknowledgments

Our manuscript benefited a lot from thorough constructive reviews by Toshiaki Tsunogae and an anonymous reviewer. This research was supported by CNEAS and FRIS of Tohoku University in part by grants from the MEXT/JSPS KAKENHI JP15H05212 and JP18H01299 to TT and JP19K04043 to KA. Ari Ganbat gratefully acknowledges the Japan ese Government MEXT Scholarship. We also thank Hironobu Harada, Isamu Morita and Taku Yutani for their assistance in laboratory.

## References

- Alessio, B.L., Collins, A.S., Siegfried, P., Glorie, S., De Waele, B., Payne, J., Archibald, D.B., 2019. Neoproterozoic tectonic geography of the south-East Congo Craton in Zambia as deduced from the age and composition of detrital zircons. *Geosci. Front.* 10 (6), 2045–2061.
- Andersen, L.S., Unrug, R., 1984. Geodynamic evolution of the Bangweulu Block, northern Zambia. *Precambrian Res.* 25, 187–212.
- Aoki, S., Aoki, K., Tsuchiya, Y., Kato, D., 2019. Constraint on the eclogite age of the Sanbagawa metamorphic rocks in central Shikoku, Japan. *Int. Geol. Rev.* 12–61, 2211–2226.
- Aoki, S., Aoki, K., Chiba, K., Sakata, S., Tsuchiya, Y., Kato, D., 2020. Origin of the Tonaru body in the Sanbagawa metamorphic belt, SW Japan. *Island Arc* 29, 2332.
- Armstrong, R.L., 1981. Radiogenic isotopes: the case for crustal recycling on a near-steady-state no-continental-growth Earth. *Philos. Trans. R. Soc. Lond. A* 443–472.
- Atherton, M.P., Ghani, A.A., 2002. Slab breakoff: a model for Caledonian, late Granite syn-collisional magmatism in the orthotectonic (metamorphic) zone of Scotland and Donegal, Ireland. *Lithos* 62, 65–85.
- Bahame, G., Manyia, S., Maboko, M.A., 2016. Age and geochemistry of coeval felsic volcanism and plutonism in the Palaeoproterozoic Ndembwa Group of southwestern Tanzania: Constraints from SHRIMP U-Pb zircon and Sm-Nd data. *Precambrian Res.* 272, 115–132.
- Begg, G.C., Griffin, W.L., Natapov, L.M., O'Reilly, S.Y., Grand, S.P., O'Neill, C.J., Hronsky, J.M.A., Djomani, Y.P., Swain, C.J., Deen, T., Bowden, P., 2009. The lithospheric architecture of Africa: Seismic tomography, mantle Petrology and tectonic evolution. *Geosphere* 5 (1), 23–50.
- Bingen, B., Jacobs, J., Viola, G., Henderson, I.H.C., Skár, Ø., Boyd, R., Thomas, R.J., Solli, A., Key, R.M., Daudi, E.X.F., 2009. Geochronology of the Precambrian crust in the Mozambique belt in NE Mozambique, and implications for Gondwana assembly. *Precambrian Res.* 170, 231–255.
- Boniface, N., 2019. An overview of the Ediacaran–Cambrian orogenic events at the southern margins of the Tanzania Craton: Implication for the final assembly of Gondwana. *J. Afr. Earth Sci.* 150, 123–130.
- Boniface, N., 2020. Geochemical Characterization of the Paleoproterozoic Massif-Type Anorthosites from the Ubendian Belt, Tanzania. *Tanzania. J. Sci.* 46, 61–75.
- Boniface, N., Appel, P., 2017. Stenian-Tonian and Ediacaran metamorphic imprints in the southern Paleoproterozoic Ubendian Belt, Tanzania: Constraints from *in situ* monazite ages. *J. Afr. Earth Sci.* 133, 25–35.
- Boniface, N., Appel, P., 2018. Neoproterozoic reworking of the Ubendian Belt crust: Implication for an orogenic cycle between the Tanzania Craton and Bangweulu Block during the assembly of Gondwana. *Precambrian Res.* 305, 358–385.
- Boniface, N., Schenk, V., 2012. Neoproterozoic eclogites in the Paleoproterozoic Ubendian belt of Tanzania: evidence for a Pan-African suture between the Bangweulu block and the Tanzania craton. *Precambrian Res.* 208, 72–89.
- Boniface, N., Tsujimori, T., 2019. Pillow lava basalts with back-arc MORB affinity from the Usagaran Belt, Tanzania: relics of Orosirian ophiolites. *J. Geol. Soc.* 176, 1007–1021.
- Boniface, N., Tsujimori, T., 2021. New tectonic model and division of the Ubendian–Usagaran Belt, Tanzania: A review and *in-situ* dating of eclogites. In: Dilek, Y., et al. (Eds.), *GSA Special Paper. The Geological Society of America* (in publication).
- Boniface, N., Schenk, V., Appel, P., 2012. Paleoproterozoic eclogites of MORB-type chemistry and three Proterozoic orogenic cycles in the Ubendian Belt (Tanzania): evidence from monazite and zircon geochronology, and geochemistry. *Precambrian Res.* 192, 16–33.
- Boniface, N., Schenk, V., Appel, P., 2014. Mesoproterozoic high-grade metamorphism in pelitic rocks of the northwestern Ubendian Belt: implication for the extension of the Kibaran intra-continental basins to Tanzania. *Precambrian Res.* 249, 215–228.
- Brock, P.W.G., 1968. Metasomatic and Intrusive nepheline-bearing rocks from the Mbozi syenite–gabbro complex, southwestern Tanzania. *Can. J. Earth Sci.* 5, 387–419.
- Bryan, S.E., Ferrari, L., Reiners, P.W., Allen, C.M., Petrone, C.M., Ramos-Rosique, A., Campbell, I.H., 2008. New insights into crustal contributions to large-volume rhyolite generation in the mid-Tertiary Sierra Madre Occidental province, Mexico, revealed by U-Pb geochronology. *J. Petrol.* 49, 47–77.
- Cahen, L., Snelling, N.J., Delhal, J., Vail, J.R., Bonhomme, M., Ledent, D., 1984. *The Geochronology and Evolution of Africa*. Oxford University Press Oxford 512.
- Cantagrel, J.M., Didier, J., Gourgaud, A., 1984. Magma mixing: origin of intermediate rocks and “enclaves” from volcanism to plutonism. *Phys. Earth Planet. Inter.* 35, 63–76.
- Chappell, B.W., White, A.J., 2001. Two contrasting granite types: 25 years later. *Aust. J. Earth Sci.* 48, 489–499.
- Cherniak, D.J., 2005. Uranium and manganese diffusion in apatite. *Chem. Geol.* 219 (1–4), 297–308.
- Chew, M.D., Spikings, R., 2015. *Geochronology and Thermochronology using Apatite: Time and Temperature, lower Crust to Surface. Elements* 11, 189–194.
- Cochrane, R., Spikings, R.A., Chew, D., Wotzlaw, J.F., Chiardia, M., Tyrrell, S., Schaltegger, U., Van der Lelij, R., 2014. High temperature (> 350 °C) thermochronology and mechanisms of Pb loss in apatite. *Geochim. Cosmochim. Acta* 127, 39–56.
- Collins, A.S., Pisarevsky, S.A., 2005. Amalgamating eastern Gondwana: the evolution of the Circum-Indian Orogens. *Earth Sci. Rev.* 71, 229–270.
- Collins, A.S., Reddy, S.M., Buchan, C., Mruma, A., 2004. Temporal constraints on Palaeoproterozoic eclogite formation and exhumation (Usagaran Orogen, Tanzania). *Earth and Plan. Sci. Lett.* 224 (1–2), 175–192.
- Condie, K.C., Bickford, M.E., Aster, R.C., Belousova, E., Scholl, D.W., 2011. Episodic zircon ages, Hf isotopic composition, and the preservation rate of continental crust. *Geol. Soc. Bull.* 123, 951–957.
- D’Agrella-Filho, M.S., Cordani, U.G., 2017. The paleomagnetic record of the São Francisco-Congo Craton. In: Heilbron, M., Alkmim, F., Cordani, U.G. (Eds.), *The São Francisco Craton and its Margins, Eastern Brazil. Regional Geology Review Series*. Springer Verlag, pp. 321–331 Chapter 17.
- Daly, M.C., 1988. Crustal shear zones in Central Africa: a kinematic approach to Proterozoic tectonics. *Episodes. J. Int. Geosc.* 11, 5–11.
- Davies, J.H., 2002. Breaking plates. *Nature* 418, 736–737.
- De Waele, B., Fitzsimons, I.C.W., 2007. The nature and timing of Palaeoproterozoic sedimentation at the southeastern margin of the Congo Craton; zircon U-Pb geochronology of plutonic, volcanic and clastic units in northern Zambia. *Precambrian Res.* 151, 95–116.

- De Waele, B., Liégeois, J.P., Nemchin, A.A., Tembo, F., 2006a. Isotopic and geochemical evidence of Proterozoic episodic crustal reworking within the Irumide Belt of south-Central Africa, the southern metacratonic boundary of an Archaean Bangweulu Craton. *Precambrian Res.* 148, 225–256.
- De Waele, B., Kampunzu, A.B., Mapani, B.S.E., Tembo, F., 2006b. The mesoproterozoic Irumide belt of Zambia. *J. Afr. Earth Sci.* 46, 36–70.
- De Waele, B., Johnson, S.P., Pisarevsky, S.A., 2008. Palaeoproterozoic to Neoproterozoic growth and evolution of the eastern Congo Craton: its role in the Rodinia puzzle. *Precambrian Res.* 160, 127–141.
- de Wit, M.J., Linol, B., 2015. Precambrian Basement of the Congo Basin and its Flanking Terrains. *Geology and Resource Potential of the Congo Basin*. Springer, Berlin, Heidelberg, pp. 19–37.
- Deblond, A., Punzalan, L.E., Boven, A., Tack, L., 2001. The Malagarazi Supergroup of Southeast Burundi and its correlative Bukoba Supergroup of Northwest Tanzania: Neo- and Mesoproterozoic chronostratigraphic constraints from Ar–Ar ages on mafic intrusive rocks. *J. Afr. Earth Sci.* 32, 435–449.
- Debruyne, D., Van Wilderode, J., Balcaen, L., Vanhaecke, F., Muchez, P., 2014. Geochemistry and isotopic evolution of the central African Domes, Bangweulu and Irumide regions: evidence for cryptic Archean sources and a Paleoproterozoic continental arcs. *J. Afr. Earth Sci.* 100, 145–163.
- Duretz, T., Gerya, T.V., 2013. Slab detachment during continental collision: Influence of crustal rheology and interaction with lithospheric delamination. *Tectonophysics* 602, 124–140.
- Duretz, T., Gerya, T.V., May, D.A., 2011. Numerical modelling of spontaneous slab breakoff and subsequent topographic response. *Tectonophysics* 502, 244–256.
- Ernst, R.E., Pereira, E., Hamilton, M.A., Pisarevsky, S.A., Rodrigues, J., Tassinari, C.C., Teixeira, W., Van-Dunem, V., 2013. Mesoproterozoic intraplate magmatic ‘barcode’ record of the Angola portion of the Congo Craton: Newly dated magmatic events at 1505 and 1110 Ma and implications for Nuna (Columbia) supercontinent reconstructions. *Precambrian Res.* 230, 103–118.
- Ernst, R.E., Hamilton, M.A., Söderlund, U., Hanes, J.A., Gladkochub, D.P., Okrugin, A.V., Kolotilina, T., Mekhonoshin, A.S., Bleeker, W., LeCheminant, A.N., Buchan, K.L., 2016. Long-lived connection between southern Siberia and northern Laurentia in the Proterozoic. *Nat. Geosci.* 9, 464–469.
- Fritz, H., Abdelsalam, M., Ali, K.A., Bingen, B., Collins, A.S., Fowler, A.R., Ghebreab, W., Hauzenberger, C.A., Johnson, P.R., Kusky, T.M., Macey, P., 2013. Orogen styles in the East African Orogen: a review of the Neoproterozoic to Cambrian tectonic evolution. *J. Afr. Earth Sci.* 86, 65–106.
- Frost, B.R., Barnes, C.G., Collins, W.J., Arculus, R.J., Ellis, D.J., Frost, C.D., 2001. A geochemical classification for granitic rocks. *J. Petrol.* 42, 2033–2048.
- Gill, R., 2011. *Igneous Rocks and Processes: A Practical Guide*. John Wiley & Sons.
- Grenholm, M., 2019. The global tectonic context of the ca. 2.27–1.96 Ga Birrimian Orogen—Insights from comparative studies, with implications for supercontinent cycles. *Earth Sci. Rev.* 193, 260–298.
- Grove, T.L., Brown, S.M., 2018. Magmatic processes leading to compositional diversity in igneous rocks: Bowen (1928) revisited. *Am. J. Sci.* 318, 1–28.
- Guo, L., Wang, T., Castro, A., Zhang, J., Liu, J., Li, J., 2012. Petrogenesis and evolution of late Mesozoic granitic magmatism in the Hohhot metamorphic core complex, Daqing Shan, North China. *Int. Geol. Rev.* 54, 1885–1905.
- Hanson, R.E., 2003. Proterozoic geochronology and tectonic evolution of southern Africa. *Geol. Soc. Lond.* 206, 427–463.
- Hartmann, L.A., Piñeyro, D., Bossi, J., Leite, J.A., McNaughton, N.J., 2000. Zircon U–Pb SHRIMP dating of Palaeoproterozoic Isla Mala granitic magmatism in the Rio de la Plata craton, Uruguay. *J. S. Am. Earth Sci.* 13, 105–113.
- Hawkesworth, C.J., Kemp, A.I.S., 2006. The differentiation and rates of generation of the continental crust. *Chem. Geol.* 226, 134–143.
- Hawkesworth, C.J., Dhuime, B., Pietranik, A.B., Cawood, P.A., Kemp, A.I., Storey, C.D., 2010. The generation and evolution of the continental crust. *J. Geol. Soc.* 167, 229–248.
- Hildebrand, R.S., Whalen, J.B., 2014. Arc and slab-failure magmatism in Cordilleran batholiths II-The cretaceous Peninsular Ranges batholith of southern and Baja California. *Geosci. Can.* 41, 399–458.
- Hildebrand, R.S., Whalen, J.B., 2017. The tectonic setting and origin of cretaceous batholiths within the north American Cordillera: the case for slab failure magmatism and its significance for crustal growth. *Geol. Soc. Am. Sp. Pap.* 532. <https://doi.org/10.1130/2017.2532> 113 pp.
- Hildebrand, R.S., Whalen, J.B., Bowring, S.A., 2018. Resolving the crustal composition paradox by 3.8 billion years of slab failure magmatism and collisional recycling of continental crust. *Tectonophysics* 734, 69–88.
- Irvine, T.N.J., Baragar, W.R.A., 1971. A guide to the chemical classification of the common volcanic rocks. *Can. J. Earth Sci.* 8, 523–548.
- Jochum, K.P., Weis, U., Stoll, B., Kuzmin, D., Yang, Q., Raczek, I., Jacob, D.E., Stracke, A., Birbaum, K., Frick, D.A., Günther, D., 2011. Determination of reference values for NIST SRM 610–617 glasses following ISO guidelines. *Geostand. Geoanal. Res.* 35, 397–429.
- Kazimoto, E.O., Schenk, V., Berndt, J., 2014a. Neoarchean and Paleoproterozoic crust formation in the Ubendian Belt of Tanzania: Insights from zircon geochronology and geochemistry. *Precambrian Res.* 252, 119–144.
- Kazimoto, E.O., Schenk, V., Appel, P., 2014b. The age of Au–Cu–Pb bearing veins in the poly-orogenic Ubendian Belt (Tanzania): U–Th–total Pb dating of hydrothermally altered monazite. *Contrib. Mineral. Petrol.* 169, 1088.
- Kazimoto, E.O., Schenk, V., Appel, P., 2015. Granulite-facies metamorphic events in the northwestern Ubendian Belt of Tanzania: Implications for the Neoarchean to Paleoproterozoic crustal evolution. *Precambrian Res.* 256, 31–47.
- Kirkland, C.L., Hollis, J., Danišík, M., Petersen, J., Evans, N.J., McDonald, B.J., 2017. Apatite and titanite from the Karrat Group, Greenland; implications for charting the thermal evolution of crust from the U–Pb geochronology of common Pb bearing phases. *Precambrian Res.* 300, 107–120.
- Kirkland, C.L., Yakymchuk, C., Szilas, K., Evans, N., Hollis, J., McDonald, B., Gardiner, N.J., 2018. Apatite: a U–Pb thermochronometer or geochronometer? *Lithos* 318, 143–157.
- Kröner, A., Stern, R.J., 2005. AFRICA| Pan-African Orogeny.
- Lawley, C., Selby, D., Condon, D.J., Horstwood, M., Millar, I., Crowley, Q., Imber, J., 2013a. Lithgeochemistry, geochronology and geodynamic setting of the Lupa Terrane, Tanzania: Implications for the extent of the Archean Tanzanian Craton. *Precambrian Res.* 231, 174–193.
- Lawley, C., Selby, D., Imber, J., 2013b. Re–Os molybdenite, pyrite, and chalcocite geochronology, lupa goldfield, southwestern Tanzania: tracing metallogenic time scales at midcrustal shear zones hosting orogenic Au deposits. *Econ. Geol.* 108, 1591–1613.
- Lawley, C.J.M., Selby, D., Condon, D., Imber, J., 2014. Palaeoproterozoic orogenic gold style mineralization at the Southwestern Archean Tanzanian cratonic margin, Lupa Goldfield, SW Tanzania: Implications from U–Pb titanite geochronology. *Gondwana Res.* 26, 1141–1158.
- Legler, C., Barth, A., Knobloch, A., Mruma, A.H., Myumbilwa, Y., Magigita, M., Msechu, M., Ngole, T., Stanek, K.-P., Boniface, N., Kagya, M., Manya, S., Berndt, T., Stahl, M., Gebremichael, M., Dickmayer, E., Repper, C., Falk, D., Stephan, T., 2015. *Minerogenic Map of Tanzania and Explanatory Notes for the Minerogenic Map of Tanzania*.
- Lenoir, J.L., Liégeois, J.P., Theunissen, K., Klerkx, J., 1994. The Palaeoproterozoic Ubendian shear belt in Tanzania: geochronology and structure. *J. Afr. Earth Sci.* 19, 169–184.
- Li, Z.X., Bogdanova, S.V., Collins, A.S., Davidson, A., De Waele, B., Ernst, R.E., Fitzsimons, I.C. W., Fuck, R.A., Gladkochub, D.P., Jacobs, J., Karlstrom, K.E., 2008. Assembly, configuration, and break-up history of Rodinia: a synthesis. *Precambrian Res.* 160, 179–210.
- Liégeois, J.P., Abdelsalam, M.G., Ennih, N., Ouabadi, A., 2013. Metacraton: Nature genesis and behavior. *Gondwana Res.* 23, 220–237.
- Maniar, P.D., Piccoli, P.M., 1989. Tectonic discrimination of granitoids. *Geol. Soc. Am. Bull.* 101, 635–643.
- Manya, S., 2012. SHRIMP zircon U–Pb dating of the mafic and felsic intrusive rocks of the Saza area in the Lupa goldfields, southwestern Tanzania: Implication for gold mineralization. *Natural Sci.* 4, 724–730.
- Manya, S., Maboko, M.A., 2016. Generation of Palaeoproterozoic tonalites and associated high-K granites in southwestern Tanzania by partial melting of underplated mafic crust in an intracontinental setting: Constraints from geochemical and isotopic data. *Lithos* 260, 120–133.
- Massawe, R.J., Lentz, D.R., 2020. Petrochemistry and U–Pb (zircon) age of porphyry dykes at the McKenzie Gulch porphyry-skarn Cu–Ag–Au deposit, north-Central New Brunswick, Canada: implications for emplacement age, tectonic setting, and mineralization potential. *Can. J. Earth Sci.* 57, 427–452.
- McCulloch, M.T., Wasserbarg, G.J., 1978. Sm–Nd and Rb–Sr chronology of continental crust formation. *Science* 200, 1003–1011.
- Meert, J.G., 2003. A synopsis of events related to the assembly of eastern Gondwana. *Tectonophysics* 362, 1–40.
- Meert, J.G., 2012. What's in a name? The Columbia (Paleopangaea/Nuna) supercontinent. *Gondwana Res.* 21, 987–993.
- Meert, J.G., Santosh, M., 2017. The Columbia supercontinent revisited. *Gondwana Res.* 50, 67–83.
- Merdith, A.S., Williams, S.E., Müller, R.D., Collins, A.S., 2017. Kinematic constraints on the Rodinia to Gondwana transition. *Precambrian Res.* 299, 132–150.
- Möller, A., Appel, P., Mezger, K., Schenk, V., 1995. Evidence for a 2 Ga subduction zone: eclogites in the Usagaran Belt of Tanzania. *Geology* 23, 1067–1070.
- Mori, K., Tsujimori, T., Boniface, N., 2018. Finding of talc-and kyanite-bearing amphibolite from the Paleoproterozoic Usagaran Belt, Tanzania. *J. Mineral. Petrol. Sci.* 113, 316–321.
- Mruma, A.H., 1989. Stratigraphy, metamorphism and tectonic evolution of the early Proterozoic Usagaran Belt, Tanzania. Ph.D thesis. University of Oulu, Finland.
- Müller, R.D., Zahirovic, S., Williams, S.E., Cannon, J., Seton, M., Bower, D.J., Tetley, M.G., Heine, C., Le Breton, E., Liu, S., Russell, S.H., 2019. A global plate model including lithospheric deformation along major rifts and orogens since the Triassic. *Tectonics* 38, 1884–1907.
- Nance, R.D., Murphy, J.B., 2019. Supercontinents and the case for Pannotia. *Geol. Soc. Lond. Spec. Publ.* 470, 65–86.
- Nance, R.D., Murphy, J.B., Santosh, M., 2014. The supercontinent cycle: a retrospective essay. *Gondwana Res.* 25, 4–29.
- Nanyaro, J.T., Ishihara, S., Hirano, H., Sasaki, A., 1983. Precambrian Granitoids from Two Areas in Western Tanzania: The Archean Bukoli Pluton and the Proterozoic Kate Batholite.
- Neves, S.P., 2011. Atlantica revisited: new data and thoughts on the formation and evolution of a long-lived continent. *Int. Geol. Rev.* 53, 1377–1391.
- Oriolo, S., Oyhantçabal, P., Wemmer, K., Siegesmund, S., 2017. Contemporaneous assembly of Western Gondwana and final Rodinia break-up: implications for the supercontinent cycle. *Geosci. Front.* 8, 1431–1445.
- Paquette, J.L., Monchoux, P., Couturier, M., 1995. Geochemical and isotopic study of a norite–eclogite transition in the European Variscan belt: Implications for U–Pb zircon systematics in metabasic rocks. *Geochim. Cosmochim. Acta* 59, 1611–1622.
- Pastor-Galán, D., Nance, R.D., Murphy, J.B., Spencer, C.J., 2019. Supercontinents: myths, mysteries, and milestones. *Geol. Soc. Lond. Spec. Publ.* 470, 39–64.
- Pearce, J.A., Peate, D.W., 1995. Tectonic implications of the composition of volcanic arc magmas. *Annu. Rev. Earth Planet. Sci.* 23, 251–286.
- Pearce, J.A., Harris, N.B., Tindle, A.G., 1984. Trace element discrimination diagrams for the tectonic interpretation of granitic rocks. *J. Petrol.* 25, 956–983.
- Pecceirillo, A., Taylor, S.R., 1976. Geochemistry of Eocene calc-alkaline volcanic rocks from the Kastamonu area, northern Turkey. *Contrib. Mineral. Petrol.* 58, 63–81.

- Pedreira, A.J., De Waele, B., 2008. Contemporaneous evolution of the Palaeoproterozoic–Mesoproterozoic sedimentary basins of the São Francisco–Congo Craton. *Geol. Soc. Lond., Spec. Publ.* 294, 33–48.
- Pidgeon, R.T., 1992. Recrystallisation of oscillatory zoned zircon: some geochronological and petrological implications. *Contrib. Mineral. Petrol.* 110, 463–472.
- Pisarevsky, S.A., Elming, S.Å., Pesonen, L.J., Li, Z.X., 2014. Mesoproterozoic paleogeography: supercontinent and beyond. *Precambrian Res.* 244, 207–225.
- Polat, A., Hofmann, A.W., 2003. Alteration and geochemical patterns in the 3.7–3.8 Ga Isua greenstone belt, West Greenland. *Precambrian Res.* 126, 197–218.
- Putirka, K., 1999. Melting depths and mantle heterogeneity beneath Hawaii and the East Pacific Rise: Constraints from Na/Ti and rare earth element ratios. *J. Geophys. Res. Solid Earth* 104, 2817–2829.
- Rainaud, C., Master, S., Armstrong, R.A., Robb, L.J., 2003. A cryptic Mesoarchaean terrane in the basement to the Central African Copperbelt. *J. Geol. Soc.* 160, 11–14.
- Rainaud, C., Master, S., Armstrong, R.A., Robb, L.J., 2005. Geochronology and nature of the Palaeoproterozoic basement in the Central African Copperbelt (Zambia and the Democratic Republic of Congo), with regional implications. *J. Afr. Earth Sci.* 42, 1–31.
- Ray, G.E., 1974. The structural and metamorphic geology of northern Malawi. *J. Geol. Soc. Lond.* 130, 427–440.
- Reddy, S.M., Collins, A.S., Mruma, A., 2003. Complex high-strain deformation in the Usagaran Orogen, Tanzania: structural setting of Palaeoproterozoic eclogites. *Tectonophysics* 375, 101–123.
- Ring, U., Kröner, A., Toulkeridis, T., 1997. Palaeoproterozoic granulite-facies metamorphism and granitoid intrusions in the Ubendian–Usagaran Orogen of northern Malawi, east-Central Africa. *Precambrian Res.* 85, 27–51.
- Ring, U., Kröner, A., Buchwaldt, R., Toulkeridis, T., Layer, P.W., 2002. Shear-zone patterns and eclogite-facies metamorphism in the Mozambique belt of northern Malawi, east-Central Africa: implications for the assembly of Gondwana. *Precambrian Res.* 116, 19–56.
- Rogers, J.J., 1996. A history of continents in the past three billion years. *J. Geol.* 104, 91–107.
- Rogers, J.J., Santosh, M., 2002. Configuration of Columbia, a Mesoproterozoic supercontinent. *Gondwana Res.* 5, 5–22.
- Rogers, J.J., Santosh, M., 2003. Supercontinents in Earth history. *Gondwana Res.* 6, 357–368.
- Rudnick, R.L., Gao, S., 2005. Composition of the Continental Crust. In: Celo, V. (Ed.), *The Crust*, pp. 1–64.
- Runcorn, S.K., 1962. Towards a theory of continental drift. *Nature* 193, 311–314.
- Salminen, J.M., Klein, R., Mertanen, S., Pesonen, L.J., Fröjdö, S., Mänttäri, I., Eklund, O., 2016. Palaeomagnetism and U-Pb geochronology of c. 1570 Ma intrusives from Åland archipelago, SW Finland—implications for Nuna. *Geol. Soc. Lond., Spec. Publ.* 424, 95–118.
- Schandlmeier, H., 1983. The geochronology of post-Ubendian granitoids and dolerites from the Mambwe area, northern province, Zambia. *Rep. Inst. Geol. Sci.* 83, 40–46.
- Schandl, E.S., Gorton, M.P., 2002. Application of high field strength elements to discriminate tectonic settings in VMS environments. *Econ. Geol.* 97, 629–642.
- Sláma, J., Košler, J., Condon, D.J., Crowley, J.L., Gerdes, A., Hanchar, J.M., Horstwood, M.S., Morris, G.A., Nasdala, L., Norberg, N., Schaltegger, U., 2008. Plešovice zircon—a new natural reference material for U-Pb and Hf isotopic microanalysis. *Chem. Geol.* 249, 1–35.
- Sommer, H., Kröner, A., Muhongo, S., Hauzenberger, C., 2005. SHRIMP zircon ages for post-Usagaran granitoid and rhyolitic rocks from the Palaeoproterozoic terrain of southwestern Tanzania. *S. Afr. J. Geol.* 108, 247–256.
- Stacey, J.T., Kramers, 1975. Approximation of terrestrial lead isotope evolution by a two-stage model. *Earth Planet. Sci. Lett.* 26, 207–221.
- Sun, S.S., McDonough, W.F., 1989. Chemical and isotopic systematics of oceanic basalts: implications for mantle composition and processes. *Geol. Soc. Lond., Spec. Publ.* 42, 313–345.
- Tack, L., Wingate, M.T.D., De Waele, B., Meert, J., Belousova, E., Griffin, B., Tahon, A., Fernandez-Alonso, M., 2010. The 1375 Ma “Kibaran event” in Central Africa: Prominent emplacement of bimodal magmatism under extensional regime. *Precambrian Res.* 180, 63–84.
- Theunissen, K., Klerkx, J., Melnikov, A., Mruma, A., 1996. Mechanisms of inheritance of rift faulting in the western branch of the east African Rift, Tanzania. *Tectonics* 15, 776–790.
- Thomas, R.J., Spencer, C., Bushi, A.M., Baglow, N., Boniface, N., de Kock, G., Horstwood, M.S., Hollick, L., Jacobs, J., Kajara, S., Kamihanda, G., 2016. Geochronology of the Central Tanzania Craton and its southern and eastern orogenic margins. *Precambrian Res.* 277, 47–67.
- Thomas, R.J., Jacobs, J., Elburg, M.A., Mruma, A., Kamihanda, G., Kankila, A., Masanja, A., Saidi, H., 2019. New U-Pb-Hf zircon isotope data for the Paleoproterozoic Ubendian belt in the Chimala area, SW Tanzania. *Geosci. Front.* 10, 1993–2006.
- Torsvik, T.H., Van der Voo, R., Preeden, U., Mac Niocaill, C., Steinberger, B., Doubrovine, P.V., Van Hinsbergen, D.J., Domeier, M., Gaina, C., Tohver, E., Meert, J.G., 2012. Phanerozoic polar wander, paleogeography and dynamics. *Earth Sci. Rev.* 114, 325–368.
- Tulibonywa, T., Manya, S., Maboko, M.A., 2015. Palaeoproterozoic volcanism and granitic magmatism in the Ngwalla area of the Ubendian Belt, SW Tanzania: Constraints from SHRIMP U-Pb zircon ages, and Sm–Nd isotope systematics. *Precambrian Res.* 256, 120–130.
- Tulibonywa, T., Manya, S., Torssander, P., Maboko, M.A., 2017. Geochemistry of the Palaeoproterozoic volcanic and associated potassic granitite rocks of the Ngwalla area of the Ubendian Belt, SW Tanzania. *J. Afr. Earth Sci.* 129, 291–306.
- van Staal, C.R., Whalen, J.B., Valverde-Vaquero, P., Zagorevski, A., Rogers, N., 2009. Pre-Carboniferous, episodic accretion-related, orogenesis along the Laurentian margin of the northern Appalachians. *Geol. Soc. Lond., Spec. Publ.* 327, 271–316.
- Veevers, J.J., 2003. Pan-African is Pan-Gondwanaland: oblique convergence drives rotation during 650–500 Ma assembly. *Geology* 31, 501–504.
- Vermeesch, P., 2018. A free and open toolbox for geochronology. *Geoscience Frontiers* 9 (5), 1479–1493.
- Whalen, J.B., Hildebrand, R.S., 2019. Trace element discrimination of arc, slab failure, and A-type granitic rocks. *Lithos* 348, 105–179.
- Wiedenbeck, M., Hanchar, J.M., Peck, W.H., Sylvester, P., Valley, J., Whitehouse, M., Kronz, A., Morishita, Y., Nasdala, L., Fiebig, J., Franchi, I., 2004. Further characterisation of the 91,500 zircon crystal. *Geostand. Geoanal. Res.* 28, 9–39.
- Wilhelmij, H.R., Cabri, L.J., 2016. Platinum mineralization in the Kapalagulu Intrusion, western Tanzania. *Mineral. Deposita* 51, 343–367.
- Xu, W.L., Ji, W.Q., Pei, F.P., Meng, E., Yu, Y., Yang, D.B., Zhang, X.Z., 2009. Triassic volcanism in eastern Heilongjiang and Jilin Provinces, NE China: Chronology, geochemistry, and tectonic implications. *J. Asian Earth Sci.* 34, 392–402.
- Yakymchuk, C., Kirkland, C.L., Clark, C., 2018. Th/U ratios in metamorphic zircon. *J. Metamorph. Geol.* 36, 715–737.
- Zen, E.A., 1986. Aluminum enrichment in silicate melts by fractional crystallization: some mineralogic and petrographic constraints. *J. Petrol.* 27, 1095–1117.
- Zhang, S., Li, Z.X., Evans, D.A., Wu, H., Li, H., Dong, J., 2012. Pre-Rodinia supercontinent Nuna shaping up: a global synthesis with new paleomagnetic results from North China. *Earth Planet. Sci. Lett.* 353, 145–155.
- Zhao, G., Sun, M., Wilde, S.A., Li, S., 2004. A Paleo-Mesoproterozoic supercontinent: assembly, growth and breakup. *Earth Sci. Rev.* 67, 91–123.